Misalignment effects on the performance and stability of x-ray free electron laser oscillator

Ganesh Tiwari[*,†] and Ryan R. Lindberg[‡]
Argonne National Laboratory, Lemont, Illinois 60439, USA

(Received 29 March 2022; accepted 25 August 2022; published 15 September 2022)

We report on the effects of transverse spatial misalignment on the performance and stability of x-ray free electron laser oscillators (XFELOs). For this study, we adopt the FEL driven paraxial resonator model in which the transverse profile of the radiation field is represented by Gauss-Hermite mode expansion. Then, we apply Gaussian optics for transporting the radiation field along with the misalignment in the optical cavity. We divide the misalignment into relevant categories of static and periodic types to understand their effects on FEL gain, lasing, and saturation. After that, we associate the first order moments of the radiation field to that of driven simple harmonic oscillator models to identify regions of instability. Throughout this report, we validate our models and analyses via theoretical calculations, analytical approximations, and simulations.

DOI: 10.1103/PhysRevAccelBeams.25.090702

I. INTRODUCTION

Recent advances for transporting coherent hard x rays with near perfect efficiency by means of Bragg crystals [1] and compound refractive lenses [2] have prompted significant activities in the research and development of x-ray free electron laser oscillators (XFELOs) [3–5]. An XFELO consists of an electron beam and an undulator as the amplifying (low gain) medium and an optical cavity containing Bragg crystals and compound refractive lenses as optical elements for circulating x-ray pulses for repetitive amplification [6,7]. A schematic layout of an XFELO is shown in Fig. 1. O represents the waist location of both electron and radiation beams. S is the undulator entrance point, and P is the exit point. The FEL radiation strikes the first optical element surface Q; it is successively guided by other cavity elements to the last optical element R, which directs the radiation beam to interact with a fresh electron beam in the undulator (SP) for further amplification. The FEL gain continues until saturation is reached in many turns.

XFELOs offer intense, stable, and coherent pulses with unprecedented spectral resolution, thereby bringing atomic laser properties to the x-ray regime [8,9]. XFELOs would benefit measurements of wide range of systems with increased accuracy (extending down to the micro eV range), improved signal counts, reduced sample damage, and reduction of exposure time of samples under study. This would enable efficient experimental studies in wide range of fields, from physics to applications in medicine, such as rare earth core materials, strongly correlated states in high temperature superconductors, atomic dynamics in disordered materials, hemoglobin mobility, and mesoscopic and artificially structured materials, and biomolecules [10,11]. Nevertheless, we are still limited in understanding the technical requirements of a realizable XFELO.

Unlike x-ray regenerative amplifier FEL [12] and similar high-gain systems, the stable operation of an XFELO relies on the quality and precise spatial and temporal alignments of both electron beams and optical cavity. Even though a complete requirement of an operable XFELO is difficult to ascertain in few numerical and/or simulation case studies, one can always determine specifications for cases where one or only a few phenomena dominate XFELO output and stability. For example, in the ideal scenario of perfect quality e-beams, an ideal undulator, and a cavity with ideal, defect-free optical elements, the stable operation of the XFELO depends on the misalignments in the cavity. In this case, we can simply model the relevant x-ray FEL physics and cavity (resonator) properties as well as the misalignments to predict the effects of misalignments on XFELO operation.

Although several FEL codes can model and simulate FELs, most like GENESIS [13] are not written with XFELO applications in mind. In addition, GENESIS discretizes the transverse profile of the radiation field on

---

[*] gtiwari@bnl.gov
[†] Present address: Brookhaven National Laboratory, Upton, New York, 11973, USA.
[‡] lindberg@anl.gov

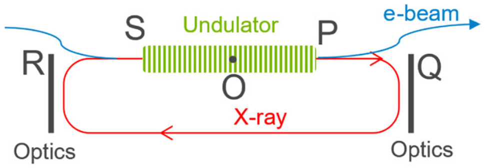

FIG. 1. Schematic of an x-ray free electron laser oscillator. The figure is not drawn to scale.

a Cartesian grid with uniform spacing resulting in the simulation run times to vary based on the desired resolution [13]. Since time-dependent FEL simulations are CPU expensive, the extension of codes like GENESIS for XFELO studies will be computationally expensive. While some codes such as GINGER [14] can simulate ideal XFELOs with Bragg crystals, conducting simulation studies of XFELOs with misalignments is outside their domain. For instance, GINGER assumes cylindrical symmetry for the transverse radiation profile [14]. This can be cumbersome for simulating XFELOs with realistic misalignments that do not respect azimuthal symmetry. To address these limitations, we adopt the free-space cavity modes–based model of the XFELO as presented in Ref. [15] to study the effects of misalignments on XFELO stability and operation. We note that the resonator modes–based model has been applied by several others before studying free electron lasers and oscillators (see Ref. [16–19]).

The rest of this report is organized as follows: In Sec. II, we introduce the cavity-based model of the XFELO, details pertaining to paraxial resonator dynamics, misalignment projections, and the impact of misalignments on single pass FEL gain. Then, we discuss our strategy for handling misalignments in simulations and present the input parameters for XFELO simulations in Sec. III. We cover the XFELO simulation results under static misalignments in Sec. IV. We evaluate unsaturated power gain values obtained from simulations and compare them to the values calculated from the Gaussian beam theory and approximate models in Sec. II D. Section V covers periodic misalignments in single and multifrequency domains. In Sec. VI, we show that the first order moments of the radiation beam behave like that of a simple harmonic oscillator driven by an external source in both static and periodic cases. After that, we investigate the instabilities set by misalignments and/or their frequencies as confirmed by the driven simple harmonic oscillator models in Sec. VII. We extend the instability analysis to calculate frequency widths/ranges of the unstable regions and their dependencies on misalignment amplitudes and quality factors of the optical cavities. Finally, we summarize our findings in Sec. VIII.

II. XFELO MODEL BASED ON CAVITY MODES

We model the XFELO using paraxial resonator modes with FEL gain, wherein the transverse profile of the circulating radiation field is represented by a Gauss-Hermite expansion, and the transport of the x-ray beam in the periodic optical cavity is computed using ray-transfer matrices including the corresponding phase advances and misalignment errors [15,20,21]. In this representation, the transverse profile of a single frequency component of the radiation beam is given by

$$E(\boldsymbol{x};z) = \sum_{l,m} \mathcal{E}_{l,m}(z) M_l(x;z) M_m(y;z), \tag{1a}$$

where

$$M_p(r;z) = \frac{\exp\left[-\frac{r^2(1-iz/z_R)}{4\sigma_r^2(1+z^2/z_R^2)}\right]}{\sqrt{2^p p! \sigma_r (1+z^2/z_R^2)^{1/2}}} \times H_p\left[\frac{r/\sigma_r}{\sqrt{2(1+z^2/z_R^2)}}\right] e^{-i(p+\frac{1}{2})\mathrm{atan}(\frac{z}{z_R})} \tag{1b}$$

is the Gauss-Hermite mode shape of the pth order, defined in terms of the spatial root mean square (rms) width σ_r, the Rayleigh range $z_R = \sigma_r/\sigma_{r'} = 2k_1\sigma_r^2$ for the paraxial field of wave number $k_1 = 2\pi/\lambda_1$ and rms divergence $\sigma_{r'}$, and the p-dependent Gouy phase shift; the mode shape functions form a complete basis set for the paraxial radiation beam and satisfy the orthonormal condition with its complex conjugate counterpart given by $\int dr\, M_p(r;z) M_q^*(r;z) = \sqrt{2\pi}\delta_{p,q}$ [20].

The Gauss-Hermite mode representation reduces the field evolution to that of the mode coefficients $\mathcal{E}_{l,m}$. These coefficients are constant under free-space propagation of the field (see Appendix A), which makes transport through the cavity relatively simple even in the presence of errors. Furthermore, since low-gain (net power gain $\lesssim 5$) FELs preferentially amplify low-order modes, the Gauss-Hermite representation is efficient in that it typically only requires $\lesssim 7$ modes in each transverse plane for accurate simulations. For convenience, we separate the radiation dynamics in the gain medium (the FEL) from that in the circulation medium (the resonator) as described in Secs. II A and II B, respectively. We also derive the single pass FEL gain for misaligned electron and radiation beams in II D.

A. FEL equations

First, we are concerned with the motion of relativistic electrons in the undulator and radiation fields. For paraxial electron beams with negligible space-charge and radiation recoil effects, the motion of the jth electron in a planar undulator field is governed by the following set of equations (see [22,23], and references within):

$$\frac{d}{dz}\theta_j = 2k_u\eta_j - \frac{k_1}{2}(\boldsymbol{p}^2 + k_\beta^2\boldsymbol{x}^2), \tag{2a}$$

$$\frac{d}{dz}\eta_j = \frac{eK[\mathrm{JJ}]}{2\gamma_0^2 mc^2}(e^{i\theta_j}E(\boldsymbol{x};z) + \text{c.c.}), \tag{2b}$$

$$\frac{d}{dz}\boldsymbol{x}_j = \boldsymbol{p}_j, \tag{2c}$$

$$\frac{d}{dz}\boldsymbol{p}_j = -k_\beta^2 \boldsymbol{x}_j, \tag{2d}$$

where an electron with arrival time t_j has the phase $\theta_j = (k_1 + k_u)z - ck_1 t_j$ in the pondermotive potential formed by the electromagnetic wave of resonant wave number k_1 and undulator with wave number k_u; the other electron coordinates are the scaled energy $\eta_j = (\gamma_j - \gamma_0)/\gamma_0$ and the transverse position and momentum $(\boldsymbol{x}_j, \boldsymbol{p}_j)$. In addition, k_β is the natural focusing in the undulator, while the energy exchange between the electron and the radiation field $E(\boldsymbol{x}, z)$ is given by the coupling in Eq. (2b), where e is the electron charge, m its mass, K is the undulator deflection parameter, and [JJ] is the Bessel function factor defined by

$$[\mathrm{JJ}] = J_0\left(\frac{K^2}{4 + 2K^2}\right) - J_1\left(\frac{K^2}{4 + 2K^2}\right).$$

Now, we shift our attention to the radiation field and its evolution. Without going into the details of this derivation (see, e.g., [22,23]), we merely quote the final form of the paraxial wave equation with FEL source current as

$$\begin{aligned}\left[\frac{\partial}{\partial z} + k_u\frac{\partial}{\partial\theta} + \frac{\nabla_\perp^2}{2ik_1}\right]&E(\theta, \boldsymbol{x}; z)\\ &= -\frac{eK[\mathrm{JJ}]k_1}{8\pi\epsilon_0\gamma_0}\frac{1}{N_\Delta}\sum_{j\in\Delta} e^{-i\theta_j}\delta(\boldsymbol{x} - \boldsymbol{x}_j),\end{aligned} \tag{3}$$

where ϵ_0 is the permittivity of free space, Δ represents the delta-slice average over an integral number of radiation wavelengths for which the field amplitude varies slowly, and N_Δ is the number of electrons in the Δ-slice. Inserting the Gauss-Hermite mode expansion from Eq. (1) into Eq. (3) and projecting onto one mode yields

$$\begin{aligned}\left[\frac{\partial}{\partial z} + k_u\frac{\partial}{\partial\theta}\right]&\mathcal{E}_{l,m}(z, \theta)\\ &= -\frac{eK[\mathrm{JJ}]k_1}{16\pi^2\epsilon_0\gamma_0 N_\Delta}\sum_{j\in\Delta} e^{-i\theta_j}M_l^*(x_j; z)M_m^*(y_j; z).\end{aligned} \tag{4}$$

In the absence of the electron beam current, the mode coefficients are constant and only slip ahead of the electron beam by one wavelength per undulator period. Finally, for ultrarelativistic electron beams used for x-ray generation, the undulator focusing is weak with $k_\beta L_u \lesssim 1$ over the undulator length L_u; for simplicity, we neglect k_β in what follows.

FIG. 2. Unfolded representation of XFELO cavity of Fig. 1. The optical axis is defined along the unperturbed ray path (red) which overlaps with that of the electron beam (blue) in the undulator.

B. Paraxial resonators

As shown in Fig. 1, the radiation beam exiting the undulator at point P during the tth turn traverses through free space and the cavity optical elements to become the input field for the $(t + 1)$th turn at the undulator entrance S. This x-ray beam transport can be achieved using any one of the several configurations of tunable or nontunable optical cavities containing different numbers of crystals and focusing elements, the simplest being a nontunable symmetric cavity that uses two focusing mirrors [24–26]. The geometric stability and loss of the radiation beam in these optical cavities can be studied using geometrical optics, in which the radiation beam is treated using paraxial rays whose passage through ideal and defect-free optical elements is described by the ray transfer matrices, often called the ABCD matrices. The general form for the transverse position (r_2) and slope (r_2') of a ray after traversing through a paraxial optical element is given by

$$\begin{bmatrix} r_2 \\ r_2' \end{bmatrix} = \mathsf{M}\begin{bmatrix} r_1 \\ r_1' \end{bmatrix} = \begin{bmatrix} A & B \\ C & D \end{bmatrix}\begin{bmatrix} r_1 \\ r_1' \end{bmatrix}, \tag{5}$$

where r_1 and r_1' are initial position and slope of the ray, respectively, and A, B, C, and D are transport components of the optical element [20,21] defined for one transverse dimension.

We assume that the radiation comes to a waist at the undulator center point O in Fig. 1, and we can trace a paraxial ray that starts at O and passes through all the optical elements to return to O, thus forming a closed loop or a round-trip. It is easier to visualize the optical cavity of Fig. 1 in the unfolded configuration as shown in Fig. 2. In this unfolded configuration, free space and flat optical surfaces constitute drift elements with their ABCD matrix given by $\left[\begin{smallmatrix} 1 & d \\ 0 & 1 \end{smallmatrix}\right]$, where d is the perpendicular distance between the ray's initial position and the optical element surface. Besides plane reflectors like Bragg crystals, XFELO cavities also consist of lenses or focusing mirrors which contribute to transverse mode matching and stability. For lenses or mirrors with large focal length f, their ABCD matrix is conveniently written as $\left[\begin{smallmatrix} 1 & 0 \\ -1/f & 1 \end{smallmatrix}\right]$. If the optical cavity consists of N elements, the round-trip of the paraxial ray starting and ending at O of Fig. 2 results in the new position and slope of the ray given by

$$\begin{bmatrix} r_2 \\ r_2' \end{bmatrix} = \mathsf{M}_N\mathsf{M}_{N-1}\ldots\mathsf{M}_2\mathsf{M}_1\begin{bmatrix} r_1 \\ r_1' \end{bmatrix} = \prod_{n=1}^{N}\mathsf{M}_n\begin{bmatrix} r_1 \\ r_1' \end{bmatrix}. \quad (6)$$

Likewise, if any optical element is misaligned, the misalignment can be propagated using a cascade of ABCD matrices from subsequent elements. Suppose the nth optical element is misaligned by $\boldsymbol{E}_n = [\begin{smallmatrix} E_n \\ F_n \end{smallmatrix}]$, where E_n and F_n refer to its respective displacement and slope errors. Then, we can write the net misalignment of the cavity representing one round-trip as [20]

$$\boldsymbol{E}_{\text{total}} = [\mathsf{M}_N\ldots\mathsf{M}_2]\boldsymbol{E}_1 + [\mathsf{M}_N\ldots\mathsf{M}_3]\boldsymbol{E}_2 + \ldots + \mathsf{M}_N\boldsymbol{E}_{N-1} + \boldsymbol{E}_N, \quad (7)$$

and the coordinates of the paraxial ray passing through this misaligned system are given by

$$\begin{bmatrix} r_2 \\ r_2' \\ 1 \end{bmatrix} = \begin{bmatrix} A & B & E \\ C & D & F \\ 0 & 0 & 1 \end{bmatrix}\begin{bmatrix} r_1 \\ r_1' \\ 1 \end{bmatrix}. \quad (8)$$

Here A, B, C, and D represent the primary ABCD components of the round-trip cavity, while E and F summarize the net cavity misalignment from the reference optical axis. From this equation, it is fairly straightforward to calculate the coordinates of the perturbed orbit and movements required for overall system alignment.

The setup of Eqs. (6) and (8) allows us to compute the stability of the periodic resonator formed by this cavity configuration as well as the effects of cavity misalignments on the radiation. For example, using eigenvalue decomposition on Eq. (6) assuming a periodic system, it is easy to show that optical cavities with $|(A+D)/2| < 1$ are stable and unstable otherwise [20]. In addition, if the cavity misalignments are static in time, we only need to calculate E and F values from Eq. (7) once to determine their effect on the paraxial rays using Eq. (8).

Now, we discuss how the ray-transfer matrix analysis can be used to understand the propagation of Gauss-Hermite modes in the optical cavity. We list the primary results here and summarize Siegman [20] to provide detailed derivations for Gauss-Hermite mode propagation through an ABCD system in Appendix B.

Stable ABCD transport through one period of length L results in a radiation phase shift that sums the usual e^{ik_1L} phase due to the path length with a contribution associated with the Gouy phase. The latter leads to a mode-dependent phase shift per turn given by

$$\frac{\mathcal{E}_n^{t+1}}{\mathcal{E}_n^{t}} = e^{-i(n+1/2)\text{sign}[\text{B}]\text{acos}[\frac{A+D}{2}]} \quad (9)$$

for each transverse dimension (see Appendix B).

For turns starting and ending at the radiation waist (which we labeled by O and assume to be at the undulator midpoint), the first order moments of a Gaussian beam at turn 2 are related to those at turn 1 by the ray-transfer matrix as follows:

$$\begin{bmatrix} \bar{r}_2 \\ \bar{r}_2' \end{bmatrix} = \begin{bmatrix} A & B \\ C & D \end{bmatrix}\begin{bmatrix} \bar{r}_1 \\ \bar{r}_1' \end{bmatrix}. \quad (10)$$

Here the bars over the terms indicate mean values with their subscripts referring to the turn number. In accelerator physics, this ray-transfer matrix and the phase advance can be represented in Courant-Snyder notation by solving Hill's equation (see Ref. [27] for example). Using the fact that $\overline{rr'} = 0$ at the waist location for periodic resonators, we can express the first order moments using

$$\begin{bmatrix} \bar{r}_2 \\ \bar{r}_2' \end{bmatrix} = \begin{bmatrix} \cos\varphi & z_R\sin\varphi \\ -\sin\varphi/z_R & \cos\varphi \end{bmatrix}\begin{bmatrix} \bar{r}_1 \\ \bar{r}_1', \end{bmatrix}, \quad (11)$$

where the Rayleigh range z_{R} replaces the particle beta function in accelerator physics, and the phase $\varphi = \text{acos}[(A+D)/2]$ is the phase advance per turn for the fundamental transverse mode. The turn at which the first order moments retrace their original or reference values for the first time is the Betatron period. Let us assume the first order moments recover their original values at Tth turn, such that $\bar{r}_T = \bar{r}_1$ and $\bar{r}_T' = \bar{r}_1'$. This implies that concatenating T single turn transport matrices yields the identity, namely, that

$$\begin{bmatrix} \cos\varphi & z_R\sin\varphi \\ -\sin\varphi/z_R & \cos\varphi \end{bmatrix}^T = \begin{bmatrix} \cos(T\varphi) & z_R\sin(T\varphi) \\ -\sin(T\varphi)/z_R & \cos(T\varphi) \end{bmatrix} = \begin{bmatrix} 1 & 0 \\ 0 & 1 \end{bmatrix}, \quad (12)$$

where the first equality follows from the generalized De Moivre's formula. Hence, the Betatron period T_β for a stable optical resonator is the turn T for which $\cos(T\varphi) = 1$, meaning that

$$T_\beta = \frac{2\pi}{\varphi} = \frac{2\pi}{\text{acos}[\frac{A+D}{2}]}. \quad (13)$$

The properties of a perfectly aligned cavity are only slightly changed under small perturbations so that the most of the previous analysis remains relevant even in the presence of misalignments. On the other hand, Eq. (8) indicates that cavity errors will lead to the nominal optical axis no longer closing upon itself, which will reduce the overlap between the electron beam and radiation, thereby reducing FEL gain. While the nominal optical axis no longer returns to itself, small perturbations result in a closed, stable orbit that defines the cold-cavity modes in the presence of misalignments [20,27]. This distorted optical axis is defined by the conditions $r_1 = r_2 = \bar{r}$ and $r_1' = r_2' = \bar{r}'$. Inserting this into (8) and solving for the distorted optical axis results in

$$\begin{bmatrix} \bar{r} \\ \bar{r}' \end{bmatrix} = (\mathbb{I} - \mathsf{M})^{-1} \begin{bmatrix} E \\ F \end{bmatrix} = \frac{1}{2 - A - D} \begin{bmatrix} (1-D)E + BF \\ CE + (1-A)F \end{bmatrix}. \tag{14}$$

The distorted optical axis defines where the stable low-gain resonator mode will be centered, while we assume that the electron beam is aligned to the nominal optical axis (0,0). Hence, the ray $(\bar{r}, \bar{r}')$ defines the overlap mismatch between the two and will be a critical tool for analyzing stability tolerances.

C. Misalignment projection

The tilt or displacement of any optical element in the cavity, including the Bragg crystals and/or the focusing lenses, acts to shift the optical axis as summarized in Eq. (14). This shifted optical axis results in coupling between cavity modes, which becomes apparent when one projects the displaced field onto the stable resonator modes at the next pass. To see how this works, let r_r and ϕ_r be the position of the displaced optical axis at the waist location; these displaced values are given by the matrix elements E and F in Eq. (8), and we consider only one dimension for simplicity. Ignoring any phase advance terms, the (new) projected one-dimensional field at the waist for the next turn $(t+1)$ will be [15]

$$E^{t+1}(r; L_u/2) = e^{ik(r-r_r)\phi_r} E^t(r - r_r; L_u/2). \tag{15}$$

Here we chose to define the undulator center at $z = L_u/2$, with L_u being the undulator length. The mode coefficients associated with the displaced field at the turn $(t+1)$ can now be related to those at turn t by inserting the Gauss-Hermite expansion and exploiting the orthonormal properties of the Gauss-Hermite modes. Multiplying both sides of Eq. (15) with the mode $M_n^*(r; L_u/2)$ and integrating over the transverse dimension r, we obtain

$$\begin{aligned} \mathcal{E}_n^{t+1}(0) &= \frac{1}{\sqrt{2\pi}} \int dr e^{ik(r-r_r)\phi_r} \\ &\quad \times \sum_l \mathcal{E}_l^t(L_u) M_l(r - r_r; L_u/2) M_n^*(r; L_u/2) \\ &= \sum_l \mathcal{E}_l^t(L_u) \mathcal{P}_{n,l}(r_r, \phi_r). \end{aligned} \tag{16}$$

The misalignment projection matrix $\mathcal{P}$ is defined in terms of associated Laguerre polynomials (first reported in Ref. [15]) as

$$\begin{aligned} &\mathcal{P}_{n,l}(r_r, \phi_r) \\ &\quad = e^{-ikr_r\phi_r/2} e^{-[(r_r/\sigma_r)^2 + (\phi_r/\sigma_{r'})^2]/8} \\ &\qquad \times \begin{cases} \sqrt{\frac{l!}{n!}} \left(\frac{iz_R\phi_r + r_r}{2\sigma_r} \right)^{n-l} L_l^{n-l} \left(\frac{r_r^2 + z_R^2 \phi_r^2}{4\sigma_r^2} \right), & [l \le n] \\ \sqrt{\frac{n!}{l!}} \left(\frac{iz_R\phi_r - r_r}{2\sigma_r} \right)^{l-n} L_n^{l-n} \left(\frac{r_r^2 + z_R^2 \phi_r^2}{4\sigma_r^2} \right), & [n \le l]. \end{cases} \end{aligned} \tag{17}$$

Hence, nonzero misalignment amplitudes act to induce phase shifts and mode couplings. For a radiation field that is initially comprised of one mode, the coupling will serve as an effective loss from that mode to others. The derivation leading to Eq. (17) is shown in Appendix C.

D. FEL gain for misaligned beams

In the low-gain regime, the solution for evolving radiation field in the FEL can be approximated and expressed in terms of the incident radiation, the spontaneous (or undulator) radiation, and the first-order field amplification, also known as gain, as derived in Ref. [22]. Upon ignoring the natural transverse focusing effect of the undulator, the power gain reduces to a simpler form in terms of the brightness functions of the undulator field $(\mathcal{B}_U)$, radiation beam $(\mathcal{B}_E)$, and electron beam $(\bar{\mathcal{F}})$

$$\begin{aligned} G = \frac{\bar{n}_e \kappa_h \chi_h}{\lambda^2} \int d\boldsymbol{\phi} d\boldsymbol{y} d\eta d\boldsymbol{x} d\boldsymbol{p} \mathcal{B}_E(\boldsymbol{y}, \boldsymbol{\phi}) \\ \times \frac{\mathcal{B}_U(\eta, \boldsymbol{x} - \boldsymbol{y}, \boldsymbol{\phi} - \boldsymbol{p}) \frac{\partial}{\partial \eta} \bar{\mathcal{F}}(\eta, \boldsymbol{x}, \boldsymbol{p}; \frac{L_u}{2})}{\int d\boldsymbol{\phi} d\boldsymbol{y} \mathcal{B}_E(\boldsymbol{\phi}, \boldsymbol{y})}, \end{aligned} \tag{18}$$

where $\bar{n}_e = I/ec$ is the peak electron line density, $\kappa_h = \frac{eK[JJ]_h}{4\epsilon_0\gamma_0}$, and $\chi_h = \frac{eK[JJ]_h}{2\gamma_0^2 mc^2}$ [22]. An explicit analytical expression has been obtained for Gaussian radiation and electron beams in Ref. [22]. To understand to what extent a given misalignment might affect the single pass FEL gain, we evaluate Eq. (18) assuming that the initial radiation and electron beams are transversely Gaussian but displaced from the optical axis in position and angle.

The brightness/distribution function of a Gaussian electron beam that is displaced at the waist in position and angle by $(\boldsymbol{r}_e, \boldsymbol{\phi}_e)$ is

$$\bar{\mathcal{F}}\left(\eta, \boldsymbol{x}, \boldsymbol{p}; \frac{L_u}{2}\right) = \frac{e^{-(\eta-\eta_0)^2/2\sigma_\eta^2}}{\sqrt{2\pi}\sigma_\eta} \frac{e^{-\hat{\boldsymbol{x}}^2/2\sigma_x^2}}{2\pi\sigma_x^2} \frac{e^{-\hat{\boldsymbol{p}}^2/2\sigma_p^2}}{2\pi\sigma_p^2},$$

where we have introduced the new variables $\hat{\boldsymbol{x}} = \boldsymbol{x} - \boldsymbol{r}_e$ and $\hat{\boldsymbol{p}} = \boldsymbol{p} - \boldsymbol{\phi}_e$, and σ_x and σ_p are rms width and divergence, respectively. Then,

$$\frac{\partial}{\partial \eta}\bar{\mathcal{F}}\left(\eta, \boldsymbol{x}, \boldsymbol{p}; \frac{L_u}{2}\right) = -\frac{\eta - \eta_0}{\sigma_\eta^2}\bar{\mathcal{F}}\left(\eta, \hat{\boldsymbol{x}}, \hat{\boldsymbol{p}}; \frac{L_u}{2}\right). \tag{19}$$

Similarly, the brightness function of a Gaussian radiation beam with input power P_{in}, rms width σ_r, and rms divergence σ_ϕ, when it is misaligned by $(\boldsymbol{r}_r, \boldsymbol{\phi}_r)$ at the waist is given by

$$\mathcal{B}_E(\boldsymbol{y}, \boldsymbol{\phi}) = P_{\text{in}}\frac{e^{-(\boldsymbol{y}-\boldsymbol{r}_r)^2/2\sigma_y^2}}{2\pi\sigma_r^2}\frac{e^{-(\boldsymbol{\phi}-\boldsymbol{\phi}_r)^2/2\sigma_\phi^2}}{2\pi\sigma_\phi^2}. \tag{20}$$

The usual undulator brightness function defined in Eq. (18) is given by

$$\mathcal{B}_U = \int_{-\frac{L_u}{2}}^{\frac{L_u}{2}} dz \int_{-\frac{L_u}{2}}^{\frac{L_u}{2}} ds\, e^{-i(2\nu\eta - \Delta\nu)k_u(z-s)} \int d\boldsymbol{\xi} \\ \times e^{-ik(\boldsymbol{x}-\boldsymbol{y}).\boldsymbol{\xi}} e^{ik[(\boldsymbol{\phi}-\boldsymbol{p}-\frac{1}{2}\boldsymbol{\xi})^2 z - (\boldsymbol{\phi}-\boldsymbol{p}+\frac{1}{2}\boldsymbol{\xi})^2 s]/2}. \tag{21}$$

With the new variables

$$\hat{\boldsymbol{x}} = \boldsymbol{x} - \boldsymbol{r}_e; \qquad \hat{\boldsymbol{p}} = \boldsymbol{p} - \boldsymbol{\phi}_e;$$
$$\hat{\boldsymbol{y}} = \boldsymbol{y} - \boldsymbol{r}_r; \qquad \hat{\boldsymbol{\phi}} = \boldsymbol{\phi} - \boldsymbol{\phi}_r;$$
$$\boldsymbol{\delta r} = \boldsymbol{r}_e - \boldsymbol{r}_r; \qquad \boldsymbol{\delta\phi} = \boldsymbol{\phi}_e - \boldsymbol{\phi}_r;$$

the 3D FEL gain formulas of Eq. (18) become

$$G = \frac{\bar{n}_e \kappa_h \chi_h}{\lambda^2} \int d\hat{\boldsymbol{\phi}} d\hat{\boldsymbol{y}} d\eta d\hat{\boldsymbol{x}} d\hat{\boldsymbol{p}} \mathcal{B}_E(\hat{\boldsymbol{y}}, \hat{\boldsymbol{\phi}}) \\ \times \frac{\mathcal{B}_U(\eta, \hat{\boldsymbol{x}} - \hat{\boldsymbol{y}} + \boldsymbol{\delta r}, \hat{\boldsymbol{\phi}} - \hat{\boldsymbol{p}} - \boldsymbol{\delta\phi}) \frac{\partial}{\partial\eta}\bar{\mathcal{F}}(\eta, \hat{\boldsymbol{x}}, \hat{\boldsymbol{p}})}{\int d\hat{\boldsymbol{\phi}} d\hat{\boldsymbol{y}} \mathcal{B}_E(\hat{\boldsymbol{y}}, \hat{\boldsymbol{\phi}})}. \tag{22}$$

Using integral formulas for Gaussian functions (in one dimension) given by

$$\int dx\, e^{-ax^2 - 2bx} = \sqrt{\frac{\pi}{a}} e^{b^2/a},$$
$$\int dx\, x e^{-ax^2 - 2bx} = -\frac{b}{a}\sqrt{\frac{\pi}{a}} e^{b^2/a}$$

and with careful calculation steps, we arrive at the following expression for the modified gain in the presence of misalignment

$$G = i\frac{j_{C,h}}{2}\frac{\sigma_x^2}{\Sigma_x^2}\int_{-\frac{1}{2}}^{\frac{1}{2}} dz \int_{-\frac{1}{2}}^{\frac{1}{2}} ds (z-s) e^{-i2(h\eta_0 - \Delta\nu/2)k_u L_u(z-s)} e^{-2[hk_u L_u(z-s)\sigma_n]^2} \\ \times \frac{\exp\left[-\frac{\boldsymbol{\delta r}^2 - \boldsymbol{\delta r}.\boldsymbol{\delta\phi} L_u(z+s) + zs(L_u\boldsymbol{\delta\phi})^2 - ikL_u(z-s)\Sigma_x^2\Sigma_\phi^2[(\boldsymbol{\delta r}/\Sigma_x)^2 + (\boldsymbol{\delta\phi}/\Sigma_\phi)^2]}{2\Sigma_x^2\left[1 + zs\frac{L_u^2\Sigma_\phi^2}{\Sigma_x^2} - i(z-s)\left(kL_u\Sigma_\phi^2 + \frac{L_u}{4k\Sigma_x^2}\right)\right]}\right]}{1 + zs\frac{L_u^2\Sigma_\phi^2}{\Sigma_x^2} - i(z-s)\left[kL_u\Sigma_\phi^2 + \frac{L_u}{4k\Sigma_x^2}\right]}. \tag{23}$$

The modified gain at harmonic h is expressed in terms of the Colson parameter $j_{C,h} = 4h\chi_h\kappa_h n_e k_u L_u^3$ and the convolved spatial and angular rms widths given by

$$\Sigma_x^2 = \sigma_r^2 + \sigma_x^2; \qquad \Sigma_\phi^2 = \sigma_\phi^2 + \sigma_p^2.$$

This gain expression reduces to the ideal gain in Ref. [22] in the absence of misalignment, namely, for $(\boldsymbol{\delta r}, \boldsymbol{\delta\phi}) = (\boldsymbol{0}, \boldsymbol{0})$.

Figure 3(a) depicts the density plot of the normalized gain for a given set of parameters listed in Table I for XFELO-A with respect to the normalized displacement and tilt errors between the radiation beam and the electron beam at the waist location in one dimension. The FEL gain stays within 80% of its ideal value provided the misalignment amplitudes are less than the rms widths, while it drops to 60% of the ideal value when the misalignments become approximately twice the rms widths of the radiation beam. Since low-gain devices like XFELO strictly depend on the FEL gain (G) and cavity losses $(1 - R)$ to satisfy the lasing condition

$$R(1 + G) \geq 1, \tag{24}$$

the prior knowledge of FEL gain dependence on misalignments is useful for identifying design tolerances for the optical cavity.

While the gain formulas [Eq. (23)] provide an analytic expression that can be numerically calculated, it may be somewhat unwieldy for simple estimates or parameter scans. To determine a simplified but approximate expression, we observe that the gain dependence on misalignment amplitude in Fig. 3(a) is reasonably Gaussian in nature and therefore propose to approximate the gain function for each dimension by

$$G_{\text{SM}} = G_0 e^{-[(\delta r/a\Sigma_x)^2 + (\delta\phi/b\Sigma_\phi)^2]/2}, \tag{25}$$

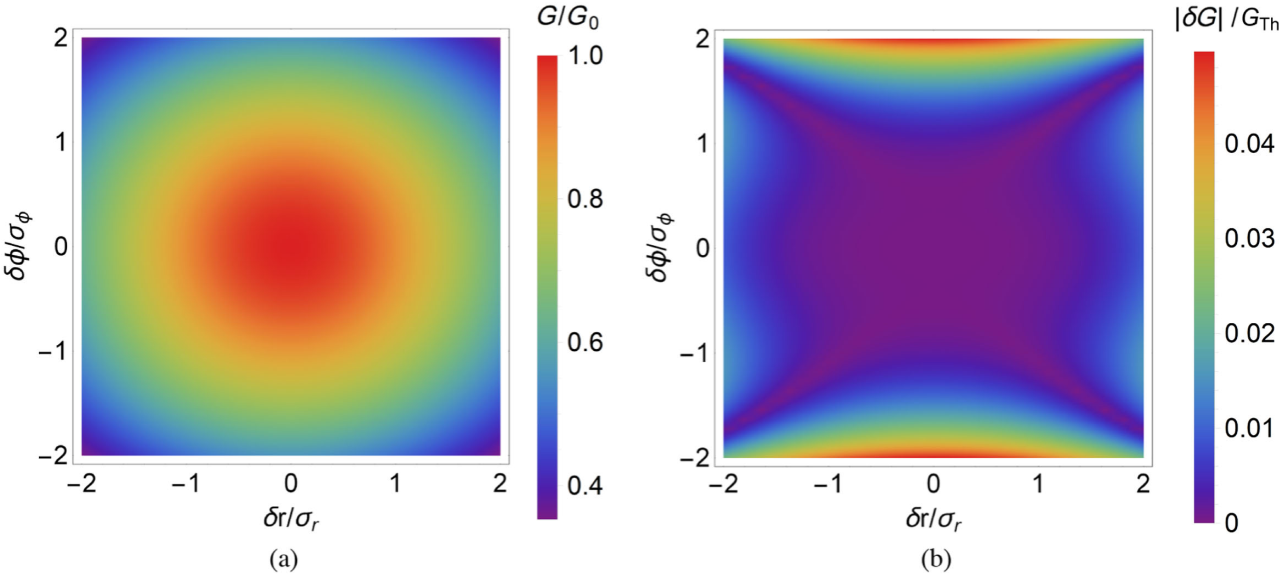

FIG. 3. (a) Density plot of (a) normalized 3D gain calculated for mismatch between radiation and electron beams at the waist location in one dimension, with error values normalized to rms widths of radiation beam, and (b) difference in normalized gain calculated from theory [Eq. (23)] and the Gaussian approximation [Eq. (25)] for a range of error values used in Fig. 3(a).

where the subscript SM indicates static misalignment, G_0 is the ideal gain value, Σ_x and Σ_ϕ are the convolved rms widths, and a and b are fit parameters to be determined. For XFELO-A, we determine the fit parameters to be $a = b \approx \sqrt{\sqrt{2}}$. For misalignment amplitudes within twice the rms size and/or divergence of the radiation beam, the approximate gain expression (25) is accurate to within 5% error of the theoretical expression in Eq. (23), as shown in Fig. 3(b). For XFELO-B, $a = 1.03$ and $b = 0.99$, whereas for XFELO-C, we estimate $a = 1.07$ and $b = 1.25$. The approximate gains estimated from these values are also found to be within 6% and 2% error of the original gain expression for misalignment amplitudes within twice the rms widths of the radiation beams for XFELO-B and XFELO-C, respectively. Later, we will apply this approximate gain model of Eq. (25) to understand features of power evolution and estimate regions of nonlasing and instabilities.

Order of magnitude tolerances can be found by setting $a = 1.09$ and $b = 1.14$, which were obtained by averaging

TABLE I. XFELO parameters for simulations.

Parameter	Symbol (unit)	A [12 keV]	B [14.4 keV]	C [9.83 keV]
Electron beam				
Energy	$\gamma_0 mc^2$ (GeV)	7	7.982	10.3
Energy spread	σ_γ (MeV)	1.4	1.5	4.35
Energy shift	δE (MeV)	2.3	3.2	7.8
Normalized emittance	ε_n (mm mrad)	0.2	0.35	0.5
Peak current	I (A)	10	100	200
Pulse length	σ_t (ps)	1	0.24	0.12
rms width	σ_x (μm)	12.67	15.054	15.73
Undulator/radiation				
Undulator periods	N_u	3000	1500	1000
Undulator length	L_u (m)	52.8	30	26
Radiation wavelength	λ_r (Å)	1.0298	0.861	1.261
Optical cavity				
Rayleigh range	Z_R (m)	10	10	10
Cavity length	L_{cav} (m)	200	300	300
Stability parameter	$\lvert A + D\rvert/2$	0.704	0.076	0.076
Ideal FEL gain	G_0	0.44	1.48	1.03

the fit parameters for all three XFELOs. Using this simplification, the Gaussian gain model has errors that are typically $\lesssim 10\%$ but may be as large as 20% when the misalignment amplitude approaches $(2\sigma_r, 2\sigma_\phi)$ the radiation beam. While this may be sufficient for initial estimates of the tolerances, the predictions were not accurate enough for our subsequent analysis, and we, therefore, resort to using fit parameter values in what follows.

III. SIMULATION SETUP

A. Approach

We extended the FEL oscillator code [15] for the cavity-based model of XFELO of Sec. II. The FEL interaction in the undulator is numerically solved with Eqs. (2a)–(2d) and (4) using the leap-frog method for symplectic integration; this ensures total (electron + radiation) energy conservation to machine precision for each pass. The misalignment of the optical elements is cascaded through the ABCD transport matrices of Eq. (7) to calculate the mean displacement and tilt of the optical axis at the waist location. Then, the mode coefficients for the start of the next pass are determined by multiplying the misalignment matrix of Eq. (17), after applying the phase advance of Eq. (9), and accounting for total cavity losses by reducing each mode coefficient value by the amount $\sqrt{1-R}$, where R is the total power reflectivity of the cavity. The XFELO simulations reported here focus on the transverse stability of the field, and are conducted using a single frequency component that effectively ignores the longitudinal effects of slippage and frequency filtering due to the Bragg crystals, and also neglects the finite angular bandwidth of the crystals. All these effects will be included in future studies. Nevertheless, we expect that the conclusions presented here will remain largely unchanged since the misalignment angles under consideration are typically $<10\%$ of the crystals' Darwin width.

In an experimental setup, misalignments occur mainly due to external sources, which also determine their nature. A displaced/tilted optic because of the alignment errors or disturbance by an experimenter is an example of static misalignment whereas a vibrating optic under the influence of motorized stages or vacuum pumps is considered periodic in nature. The effects of vibrational noises resulting from cultural-technical noise and ground motion in accelerators have been studied in detail through measurements and modeling [28–31]. Since XFELOs are expected to operate at frequencies between a few hundred kHz and a few MHz and reach saturation within a few hundred to thousand turns, the effects of cultural-technical and ground vibrations up to few hundred Hz with associated rms displacements between 0.1 μm and 1 nm are not of major concern for XFELO stability and operation [32,33]. Nevertheless, our interest lies in identifying scenarios that would hinder XFELO saturation for a better understanding and predictability of the misalignment effects. Following [15], we separate the misalignments cases into three categories: (a) static—the cavity optics are misaligned at a fixed value for all passes/turns, (b) periodic—misalignments are pass-dependent, but sinusoidal or periodic in time, and (c) random—pass-dependent and realistic like scenario but neither fixed nor periodic.

B. Input parameters

We consider three XFELOs listed in Table I. XFELO-A employs a relatively long bunch with low peak current that would minimize deleterious wakefields and whose parameters could be achieved in an energy recovery linac. The electron beams for XFELO-B and XFELO-C have higher peak currents and shorter bunch lengths and target different x-ray wavelengths; the remaining parameters are chosen to provide an FEL gain between 0.4 and 1.5 while being consistent with what high-brightness injectors and permanent magnet undulators can achieve.

The cavity configurations of the XFELOs are shown in Fig. 4. XFELO-A uses a two crystal and two focusing mirror configuration [Fig. 4(a)], where the undulator is positioned directly between the flat crystal mirrors that are separated by 98 m. The focusing mirrors, each with 26.0 m focal length, are placed 1.0 m after the crystals and are separated from each other by 100 m. Hence, the total cavity length is 200 m which, together with the focusing mirrors, defines a stable mode whose waist is at the center of the undulator and whose Rayleigh range is 10 m. For this cavity, $A = D \approx 0.704$, so that the Betatron period $T_\beta = 2\pi/\mathrm{acos}[(A+D)/2] \approx 7.96$ turns. XFELO-B and

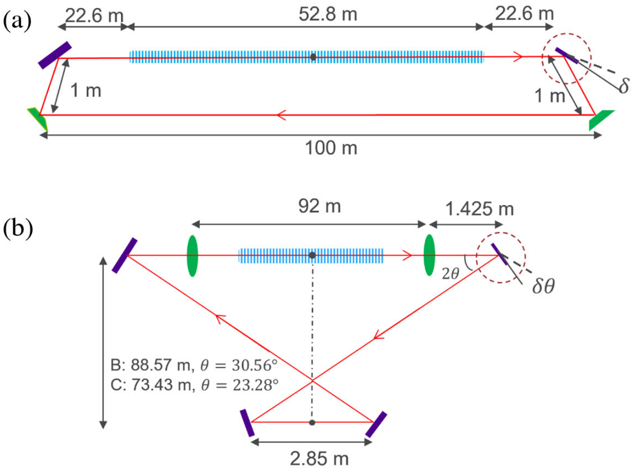

FIG. 4. XFELO cavity configurations based on (a) two focusing mirrors (green) and two flat crystals (purple) for XFELO-A, and (b) two compound refractive lenses (green) and four crystals (purple) forming a bow-tie pattern for XFELO-B (with $\theta =$ 30.56° for C444 crystal) and XFELO-C (with $\theta = 23.275°$ for C333 crystal). Figures are not drawn to scale. For (a), the geometrical shape is only approximate and determined by the choice of crystals and focusing mirrors.

XFELO-C use a tunable, bow-tie cavity configuration with four crystals and two focusing lenses as shown in Fig. 4(b). The focal length of each lens is 36.73 m and are separated from each other by 92 m to define a Rayleigh range of 10.0 m at the undulator center in the cavity. The total cavity length is 300 m and a second waist with a Rayleigh range of 72.58 m exists at the center of two crystals separated by 2.85 m. For both XFELO-B and XFELO-C, $A = D \approx -0.0759$ defining a Betatron period of ≈3.82 turns. XFELO-B uses C444 crystals with an incident angle of 30.56°, whereas XFELO-C utilizes C333 crystals at an incident angle of 23.275°. We note that alternate crystal choices with a slight change in cavity parameters may allow better angular acceptance. For example, using C444 results in full width at half maximum (FWHM) angular acceptance of only 2.4 μrad, whereas using C337 at an incident angle of 9.17° offers FWHM Darwin width of 4.0 μrad. Similarly, the tuning range for an XFELO using the C333 reflection was found to be only 6% in a previous study [32].

We assume that the nominal power loss per turn is 20% and define the cold-cavity efficiency in terms of the ratio of stored power to power loss per turn via $\hat{q} = R/(1-R)$, where $\hat{q}$ is related to the standard Q factor of the optical resonator as $Q = 2\pi\hat{q}/R$. For all simulations and calculations presented in this report, we ignore the natural transverse focusing from the undulator and consider misalignments only in one transverse direction, generated by tilting and/or displacing the first crystal as shown in Fig. 4. The seeding pulse is a weak signal fundamental transverse mode and the electron shot noise (spontaneous radiation emission) is turned off. We choose XFELO-A for detailed analysis and comparisons in Secs. IV–VI to demonstrate the response characteristic of low-gain FEL oscillators under various misalignments.

IV. STATIC MISALIGNMENTS

We simulate static misalignment by tilting and/or displacing the first crystal in the cavity and propagate the effect of the misalignment to the center of the undulator using ray-matrix transfer analysis. This then serves as the input displacement in position and angle for the misalignment projection formula derived in Sec. II C. As an example, for the cavity in Fig. 4(a) crystal tilt of −45 nrad results in the radiation beam being shifted from the waist transversely by 0.413 of its rms size and in angle by 0.276 of its rms divergence. We obtain a similar position offset at the waist from tilting the second crystal by roughly 40 nrad.

Equation (14) tells us that tilting the first crystal by −45 nrad results in a closed optical axis that is displaced by the coordinates $(-0.124\sigma_r, 0.634\sigma_\phi)$ from the nominal axis. In the absence of gain or loss, the radiation freely oscillates about the closed optical axis at the Betatron frequency. Including FEL gain and cavity loss drives the radiation beam toward a steady state, and this steady state is located between the cold-cavity equilibrium (i.e., the distorted closed orbit) and the nominal optical axis where the gain is maximized. For our low-gain system, we find that the steady state is closely approximated by the distorted closed orbit. Figure 5(a) shows the evolution of radiation beam centroid phase space for four cases of constant crystal tilts representing the approach to steady state through power saturation in XFELO-A. The FEL simulations indicate radiation beam settling close to coordinates predicted by Eq. (14). For instance, a crystal tilt of −45 nrad led to a steady-state orbit with coordinates $(-0.069\sigma_r, 0.639\sigma_\phi)$, not far from the theoretical value of $(-0.124\sigma_r, 0.634\sigma_\phi)$ obtained from Eq. (14). While we found the major perturbation (slope error in this case) affecting FEL gain is close to the value predicted by ABCD analysis for all cases considered in Fig. 5, our simulations indicate the mean positions of the radiation beam settled at values half of that predicted by ABCD analysis. We assume this effect stems from FEL dynamics and gain compensation.

Figure 5(b) shows the evolution of the total intracavity power for constant crystal tilts up to 0.125 μrad. The outcoupled power for this case would be about 6% of what is shown, meaning that a perfectly aligned cavity results in ~0.8 MW for users. Increasing the crystal tilt leads to larger offsets between the radiation beam and the electron beam and thus, less transverse area for FEL interaction and reduced gain per pass. This results in longer buildup times for saturation as well as lower saturated powers. Additionally, the buildup time and saturation power can be further impacted by angular filtering of the crystals, and this deleterious effect becomes more significant for reflection angles different from near normal where the crystal angular acceptance decreases.

While misalignments affecting XFELO performance are not desired in general, small residual misalignments inevitably occur in experimental setups. We have shown that such nonideal cavity conditions lead to suboptimal performance and are now in the position to use this information to set tolerances on the alignment errors. For instance, since the XFELO of Fig. 5(b) showed little change in gain or saturation power for crystal tilts less than 20 nrad, we conclude that achieving an angular alignment tolerance less than this will result in high-quality output. If we allow ourselves ~10% reduction in output power, then the tolerance grows to 45 nrad. Generalizing this last result to the entire cavity, we find that a combination of static misalignments that result in steady-state radiation beam offsets at the waist by less than $(-0.07\sigma_r, 0.64\sigma_\phi)$ will have negligible effects on gain and $\lesssim 12\%$ effect on saturated power.

A static misalignment can cripple an XFELO if gain is reduced below its threshold value

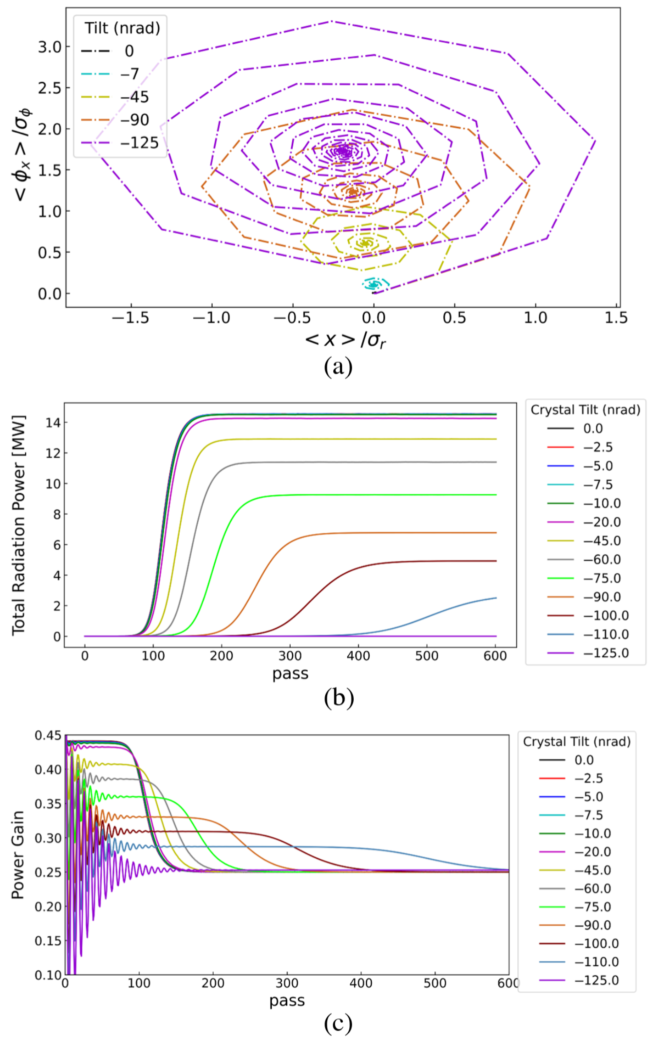

(a)

(b)

(c)

FIG. 5. Evolution of (a) transverse centroid phase space of the radiation beam at the waist along the misalignment dimension, (b) total radiation power, and (c) radiation power gain per pass for constant crystal tilts from 0 to 125 nrad in the first crystal of XFELO-A defined by Table I and Fig. 4(a).

$$G_{\mathrm{thres}} = \frac{1-R}{R} = \frac{1}{\hat{q}}.$$

We expect that this threshold will be reached when the misalignment leads to a steady-state radiation beam offset exceeding the rms width of the radiation or electron beam (whichever is smaller). For the case in Fig. 5(b), the gain becomes zero when the crystal tilt approaches 125 nrad, which from Fig. 5(a) corresponds to a steady-state displacement of the stable optical mode by approximately $(-0.187\sigma_r, 1.721\sigma_\phi)$. At this stage, the single pass FEL gain is predicted by the theory to drop by more than 35% according to Eq. (23) [Fig. 3(a)].

For misalignments that lead to displacements between the two extremes of ideal and zero gain, we plot the FEL gain per pass obtained from the simulation in Fig. 5(c). Initially, the gain appears to oscillate, which is an artifact of the initial seed field not being matched to the steady-state mode along the distorted closed orbit. After the initial oscillating transient, the FEL gain settles to a nearly constant value during which the field grows exponentially. We observe that this unsaturated FEL gain, by which we mean the gain during the exponential growth region, decreases as the misalignment amplitude increases. We compare the simulation results to analytical gain calculations in Fig. 6, where the theory computes the gain from the simulated steady-state position and angular displacements. The simulated and analytical FEL gain follows a similar downward trend with increasing misalignment amplitude, with very good agreement for crystal tilts up to 45 nrad, and increasing deviations that still stay within 10% up to the crystal tilt of 110 nrad. The simplified theory based upon the Gaussian approximation converges with the theory for all misalignment amplitudes that do not sabotage lasing and XFELO saturation as we indicated earlier in Sec. II D. The approximate Gaussian model starts to diverge from the theory at 125 nrad crystal tilt amplitude, the region where the XFELO cannot sustain lasing anymore.

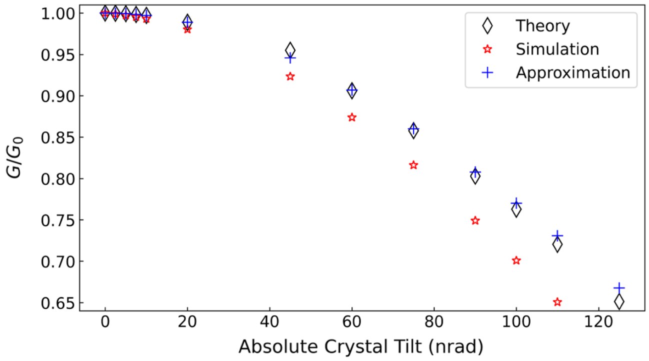

FIG. 6. Comparison of normalized gain values obtained from simulations, calculated gain formulas of Eq. (23), and approximate gain formulas of Eq. (25) for steady-state coordinates of the radiation beam obtained from simulations.

In addition to the exponential growth, Fig. 5(c) also shows how the FEL gain saturates due to nonlinear interactions with the beam. A convenient model for the XFELO power/intensity buildup to saturation can be formulated in the form of (see Ref. [20] and references within for more details)

$$\frac{dP}{dn} = (\delta_m - \delta_c)P - \frac{2\delta_m}{P_{\mathrm{sat}}}P^2, \tag{26}$$

where $\delta_m = \ln(1+G)$ corresponds to the unsaturated growth rate, $\delta_c = \ln(1/R)$ is the rate of power loss, and P_{sat} is the power at saturation. The above equation has an exact analytical solution given by

$$P(n) = \frac{P_0 P_{ss} e^{n(\delta_m - \delta_c)}}{P_{ss} + P_0[e^{n(\delta_m - \delta_c)} - 1]},$$
$$P_{ss} = \left(1 - \frac{\delta_c}{\delta_m}\right)\frac{P_{\mathrm{sat}}}{2} \tag{27}$$

For the ideal case, the saturated power is approximated as $P_{\mathrm{sat}} = \frac{P_{\text{e-beam}}}{2\delta_c N_u} = \frac{I\gamma_0 mc^2}{e 2\delta_c N_u}$ [22]. For the low-gain XFELO under study with a high-quality cavity, we can use approximations $\delta_m \approx G$ and $\delta_c \approx 1 - R$. From simulations shown in Fig. 5(b), the power at steady state in the ideal case is $P_{\mathrm{ss}}^{\mathrm{sim}} = R \times 14.4934 = 11.595$ MW. Since the ideal gain calculated from Eq. (23) for Gaussian beams is $G_0 = 0.378$, we estimate the power at the steady state to be $P_{\mathrm{ss}}^{\mathrm{th}} \approx 13.74$ MW, which is a good approximation. We note that analytical models represented by Eqs. (23)–(27) can be useful for quick preliminary analysis of XFELOs considered under static misalignment.

V. PERIODIC MISALIGNMENTS

Misalignments in an operational XFELO will vary over time due to a variety of causes from slow drifts to vibrations from noise sources across the frequency spectrum. Small variations with frequencies less than 100 Hz, which is typical of both ground motion and cultural-technical noise, can easily be eliminated with active feedback (see, e.g., [34]). Vibrations that lead to misalignments over time scales of 0.1 to 10 kHz can also in principle be controlled with advanced feedback techniques, while any misalignment occurring at the 10 to ∼500 kHz will probably have to be limited to levels such that XFELO performance is not adversely affected. Noise in the latter two frequency ranges can come from many sources, including e-beam jitter, cavity detuning effects, piezo-actuators malfunctions, mechanically undamped turbo pumps, and sudden movements of experimental setup due to ground motions, construction works, and so on. In general, all sources of noise contribute, with the total effect typically described by the power spectral density of fluctuations. Nevertheless, we can learn about how much time-varying misalignments affect XFELO output by investigating the response to oscillations that have one or two frequency components. To this end, we model periodic crystal tilt error at pass t using

$$\delta\theta(t) = \sum_{i=1}^{N} (\delta\theta)_i \cos(\omega_i t), \tag{28}$$

where $(\delta\theta)_i$ is the misalignment amplitude imparted by the source associated with frequency ω_i. For now, we limit our studies to misalignments with frequencies less than the Betatron frequency, $\omega_i < \omega_\beta$.

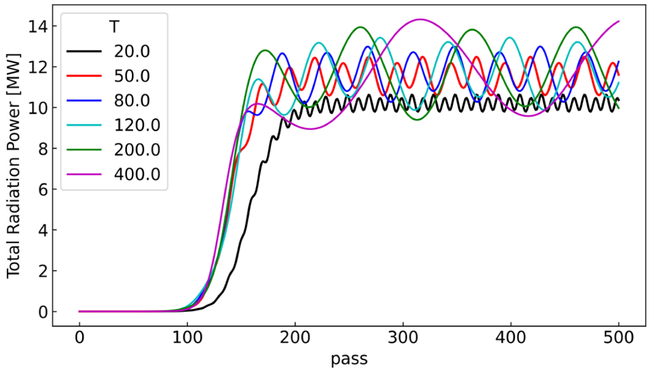

FIG. 7. Evolution of total radiation power per pass for periodic misalignment with the crystal tilt modeled as a sinusoid given by $\delta\theta(t) = \delta\theta \cos(\omega t)$ for six different frequencies in XFELO-A. The label T indicates the period in turns associated with each frequency.

A. Single frequency

Single frequency simulations allow us to investigate how the output power fluctuations depend upon the time scale over which the misalignment varies. Figure 7 shows the power evolution in XFELO-A for a wide range of single-frequency misalignment. The period of these misalignments ranges from 20 to 400 turns with the misalignment amplitude corresponding to −75 nrad crystal tilt. The power buildup at the steady state shows two-fold behavior in sampling frequency. This two-fold frequency feature of power evolution can be understood using the approximate Gaussian gain of Eq. (25). For periodic misalignments of a single frequency defined by expression (28), the mean position of the radiation beam at steady state is directly proportional to the driving amplitude, i. e., $\bar{r}(t) \propto \delta r \cos(\omega t)$, where δr is the steady-state displacement value. Upon substituting $\bar{r}(t) = c_r \delta r \cos(\omega t)$ and $\bar{\phi}(t) = c_\phi \delta r \cos(\omega t)$, the approximate gain for this sinusoidal misalignment at tth pass takes the following form

$$G_p(t) = G_0 e^{-\cos^2(\omega t)[(c_r \delta r/\Sigma_x)^2 + (c_\phi \delta\phi/\Sigma_\phi)^2]/2\sqrt{2}}$$
$$= \sqrt{G_0 G_{\mathrm{SM}}} e^{-\rho \cos(2\omega t)/2},$$

where we used the trigonometric identity for cosine function, G_{SM} is the gain for the static misalignment case, and we introduced

$$\rho = [(c_r \delta r/\Sigma_x)^2 + (c_\phi \delta\phi/\Sigma_\phi)^2]/2\sqrt{2},$$

c_r and c_ϕ are constants of proportionality. In Sec. VI, we will show that these constants represent frequency-dependent responses. The exponential part carries $\cos(2\omega t)$ indicating that the misalignment frequency gets doubled for gain and power. Since Nyquist frequency is 750 kHz for XFELO-A, misalignment occurring at frequencies above 375 kHz will be aliased to smaller frequencies in power evolution.

In addition, we observed suppression of power fluctuations after saturation with increasing frequency (decreasing period) in Fig. 7. The periodic variations that occur on the timescale much longer than the cavity round-time imprint themselves upon the output, whereas the fluctuations with smaller timescales are averaged over the full amplitude oscillations for a given misalignment amplitude. While the general periodic behavior seen in Fig. 7 mirrors that previously published in Ref. [15], the saturated power values are somewhat different. This difference is due to the effect of the turn-by-turn mode-dependent Guoy phase shift of Eq. (9) that was not properly accounted for in Ref. [15].

Returning to Fig. 7, we see that the oscillation amplitude decreased by half for the misalignment period of 80 turns when compared to that of 400 turns. The further increase in the misalignment frequency (to a period of 20 turns) led to a further reduction in the power fluctuations. At this frequency, we observe a further decrease in unsaturated FEL gain during the exponential growth regime (100–200 turns), and hence, the reduction in average power output by $\geq 10\%$ compared to lower frequency cases. We will cover the cases with frequencies close to the Betatron frequency that lead to excitations, poor performance, and even instabilities in Sec. VI and beyond.

B. Multiple frequencies

In real systems, misalignments originate from various sources that contribute over a wide range of frequencies, whose total effect can be taken into account via Eq. (28). While such modeling will be needed for any particular facility once the noise sources are known, we think that an exhaustive study of the many scenarios would be both challenging to complete and difficult to interpret. Rather, we study the response to periodic misalignments that have only two or three frequency components. We find that the resulting power evolution is essentially a superposition of the single frequency responses, and therefore conclude that the single frequency response gives important information regarding generic, time-varying errors. While this observation may seem reasonable, it is perhaps not obvious due to the nonlinear nature of the FEL at saturation.

For simplicity, we consider a case where both frequencies occur with the same misalignment amplitude. In this case, the centroid of the misaligned radiation beam evolves as

$$\bar{r}(t) = c_r \frac{\delta r}{2}[\cos(\omega_1 t) + \cos(\omega_2 t)]$$

at the steady state, and the approximate gain at the tth turn becomes

$$G_p(t) = G_0 e^{-\rho[2+\cos(2\omega_1 t)+\cos(2\omega_2 t)]/8} \times e^{-\rho\cos[(\omega_1+\omega_2)t]/4} e^{-\rho\cos[(\omega_1-\omega_2)t]/4}. \tag{29}$$

In addition to the responses at $2\omega_1$ and $2\omega_2$, we find that the gain also contains the beat frequencies $\omega_1 \pm \omega_2$. The exponential containing the individual responses at twice the frequencies in the first line indicates that the gain will fluctuate between G_0 and $G_0 e^{-\rho/2}$. Since the contribution from the exponential containing the sum of frequencies is $e^{\pm\rho/4}$ (maximum/minimum) at constructive interference, this results in the shift of gain fluctuation between $G_0 e^{-3\rho/4}$ and $G_0 e^{\rho/4}$. However, further truncation from the exponential containing the difference of frequencies reduces the maximal achievable gain to G_0 because it also contributes a factor of $e^{\mp\rho/4}$ at minimum/maximum when constructive interference occurs. In other words, Eq. (29) indicates that the gain fluctuates between G_0 and $G_0 e^{-\rho}$ in the presence of two frequencies. These beat frequencies will also be present in the saturated power, but the high frequency oscillation $(\omega_1 + \omega_2)$ will be less prominent since it will be more strongly averaged (damped) by the cavity Q resulting in reduced power fluctuations as we observed earlier in Fig. 7.

The difference frequency has a period of $2\pi/|\omega_1 - \omega_2|$ turns, and we will observe features of constructive interference in the steady-state power fluctuations at intervals given by

$$T_C = \frac{\pi}{\omega_1 - \omega_2} = \frac{T_1 T_2}{2|T_2 - T_1|}, \tag{30}$$

and destructive interference occurring at the same interval but shifted by $\sim T_C/2$ passes. In other words, each period in the difference frequency contains two constructive interference and four destructive interference patterns. One constructive interference leads to amplification of gain (at destructive interference) by $e^{\rho/4}$ whereas the other one leads to attenuation by the same factor. Figure 8(a) shows the power evolution per pass for crystal oscillations with two frequencies of oscillation, where the second period is fixed at 80 turns and the crystal tilt amplitude is -37.5 nrad for both frequency components. For the most rapid oscillation with $T_1 = 20$, the period $T_C \approx 13.3 \sim T_1$ is difficult to clearly identify, and furthermore the gain and cavity Q more effectively average over the relatively high frequency oscillations, which leads to less variation in the power. When $T_1 = 50$, 64, and 100, however, the respective periods of constructive interference $T_C \approx 67$, 160, and 200 are clearly visible in the power. For $T_1 = 50$, we observe three peaks due to gain amplification at 200, 333, and 467 turns followed by dips due to gain attenuation halfway between them. The peaks for $T_1 = 64$ occur at 160 and 480 turns with a power dip following at 320 turn. Similar trends are found for $T_1 = 100$ at 200, 400, and 600 turns. The maximum intracavity power in these regions of

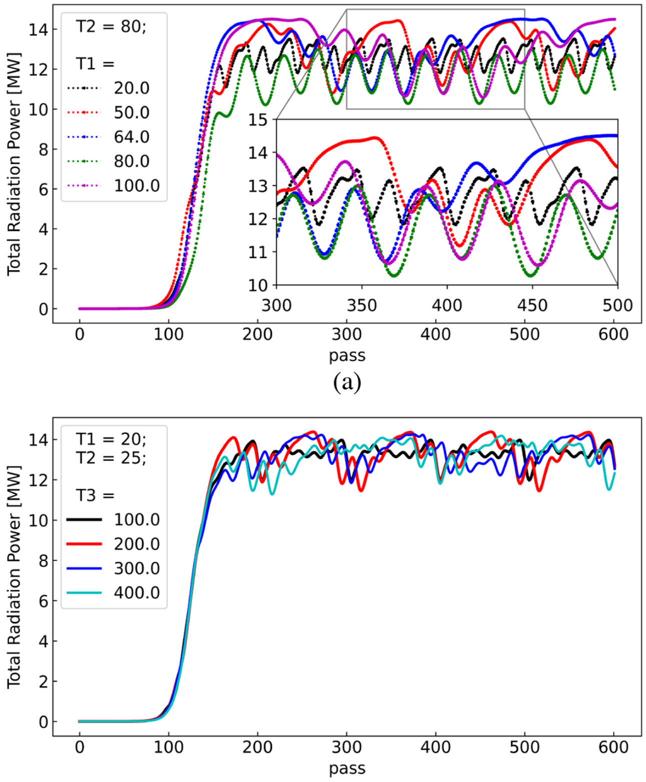

(a)

(b)

FIG. 8. Evolution of total radiation power per pass for scans conducted (a) for two frequencies with the second frequency component kept fixed with its period at 80 turns, and (b) for three frequencies with two frequencies kept fixed close to each other with their periods corresponding to 20 and 25 turns.

constructive interference approaches the ideal, steady-state value ≈14.5 MW, while the power in between is close to that when both frequencies are equal as depicted by the green line of Fig. 8(a). Hence, the average power at steady state is larger when $T_1 \neq T_2$. In fact, for disparate frequencies, we expect the average power to be dictated by the rms average over the two misalignment amplitudes, which in this case, is reduced by a factor of $\sqrt{2}$.

We observe similar features for the particular case of three frequencies provided the gap between two of the frequencies is much smaller than their difference from the third frequency, namely, either $(\omega_1, \omega_2 \ll \omega_3)$ or $(\omega_1, \omega_2 \gg \omega_3)$. In this case, the dominating beat frequency occurs with the periodicity

$$T_C = \frac{\pi}{\omega_1 + \omega_2 - 2\omega_3} = \frac{T_1 T_2 T_3}{|T_3(T_2 + T_1) - 2T_1 T_2|}. \tag{31}$$

Again, the periodic "constructive interference" leads to times when the FEL gain and output power that is close to the unperturbed state, while there are other times within the difference period for which the gain and power will be somewhat attenuated. Furthermore, we expect that the phenomenology of the three frequency cases just described will become almost indistinguishable from the two frequency cases in the limit that the misalignment amplitudes associated with the first two frequencies are equal and half that associated with ω_3.

Figure 8(b) shows the power evolution profile in the presence of three frequencies under the previous constraints. The misalignment amplitude for T_3 is set at −37.5 nrad crystal tilt while that of T_1 and T_2 are at −18.75 nrad tilt. From the expression (30), we expect the gain amplification/attenuation by constructive interference to occur at every 50 turns between $T_1 = 20$ and $T_2 = 25$. For $T_3 = 100$, we expect constructive interference to occur at every 14.29 turns from Eq. (31). We only observe the maxima/minima in power fluctuations at turns when integer multiple of 14.29 turns (every 100 turns) equals the integer multiple of the period of constructive beats between two frequencies occur. In this case, such occurrence is observed every 100 turns as shown in Fig. 8(b). Similar patterns emerge for $T_3 = 200$, 300, and 400. Moreover, the damping of higher frequency components is also evident.

VI. HARMONIC OSCILLATIONS

So far, we have focused on a few cases of static and periodic misalignments, concentrating on the gain, the power buildup, and the final saturated power. Now, we shift our attention to the evolution of the first order moments, how they can be modeled using a simple harmonic oscillator model, and this model's application to assessing potential instabilities.

The solid lines in Figs. 9(a) and 9(b) show the mean position and divergence of the radiation beam minus their steady-state values at the waist location plotted against the pass for the static misalignment cases of Fig. 5; the centroids execute damped oscillations with a frequency close to Betatron frequency before approaching the steady state. This makes physical sense since we have already established that a misaligned cavity has an equilibrium about the distorted closed orbit, a natural frequency ω_β, and loss due to the reflectivity $R < 1$. Hence, we model the radiation centroid using the following damped harmonic oscillator equation:

$$\frac{d^2}{dt^2}\bar{y} + 2\beta\frac{d}{dt}\bar{y} + \omega_\beta^2\bar{y} = \omega_\beta^2\delta y, \tag{32}$$

where the natural frequency is the Betatron frequency ω_β, the damping factor is β, and the steady-state amplitude is the driving amplitude δy which corresponds to the closed orbit at the cavity center. The solution for the centroid is then

$$\bar{y}(t) = \delta y + \frac{(y_0 - \delta y)e^{-\beta t}}{\cos\psi}\cos\left(t\sqrt{\omega_\beta{}^2 - \beta^2} + \psi\right) \tag{33}$$

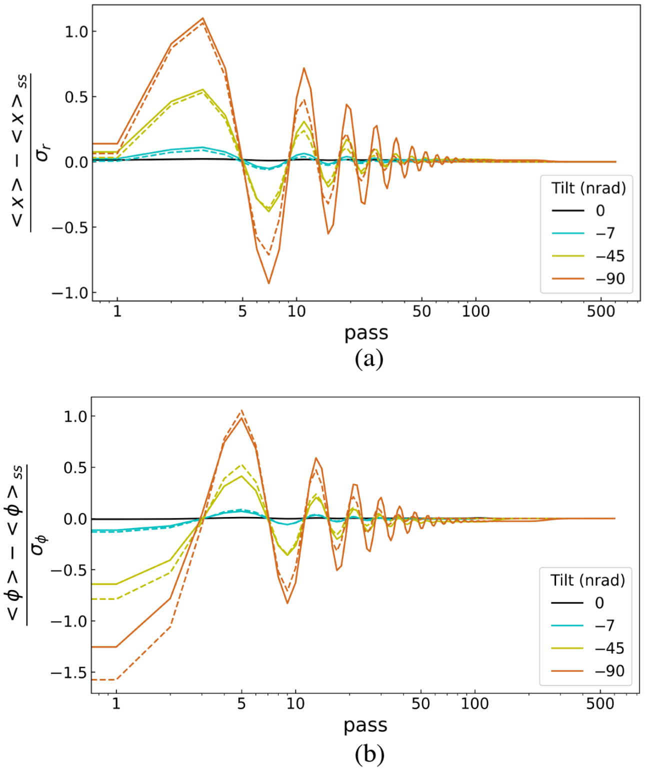

(a)

(b)

FIG. 9. Plot of (a) mean position and (b) mean divergence of the radiation beam minus their steady-state values versus pass for static misalignment cases of Fig. 5 obtained from the simulations (solid lines) and harmonic oscillator model of Eq. (32) (dashed lines). The x-axis scale is $\log_{10}$.

where the phase ψ is determined by the initial condition, with $\tan\psi = [\frac{y_0'}{\delta y - y_0} - \beta]/\sqrt{\omega_\beta^2 - \beta^2}$ for $\bar{y}(0) = y_0$ and $\bar{y}'(0) = y_0'$. The displacement at the steady state is given by the first term δy, while the second term describes the transient evolution wherein the centroid makes damped oscillations with the frequency $\sqrt{{\omega_\beta}^2 - \beta^2}$ like those seen in Figs. 9(a) and 9(b) [35]. We expect the damping factor β to scale with radiation amplitude loss in the cavity, i.e., $\beta \propto (1 - R)$. We verified this by conducting scans using cavities with Betatron periods between 4 and 20 turns and also for different FEL gains (≤ 2) and power loss per turn. We concluded that $\beta \approx (1 - R)/2$ based upon these scans.

We show the harmonic oscillator solutions of Eq. (33) for mean position and divergence minus their steady-state values over pass with the dashed lines in Figs. 9(a) and 9(b), respectively. The initial displacement values used for the dashed lines were obtained using ABCD matrix analysis [Eq. (8)], whereas we used the steady-state values from the simulations for consistency. The overlap between the simulations and the harmonic oscillator model results are obtained for the damping factor $\beta = (1 - R)/2$ and also by shifting the dashed lines right by 2.7 turns for mean position and 7 turns for mean divergence. Since the simulation is conducted with a weak seeding pulse of fundamental transverse mode in which the evolving radiation beam after each turn suffers constant misalignment, the coordinates of the radiation beam after the first pass or even first few passes do not necessarily converge immediately to the values predicted by ray-transfer matrix analysis, thereby justifying the applied shift correction. The overall phenomena of transient damped oscillations of the first order moments on the approach to steady state is effectively captured by the simple harmonic oscillator model as observed in Fig. 9. In addition, the early excitation amplitudes for mean position are found to occur at $t = \frac{(2n+1)\pi}{\sqrt{\omega_\beta^2 - \beta^2}}$, where $n = 0, 1, 2, 3, \ldots$ based on Eq. (33). The first excitation occurs for $n = 0$, and $t = \frac{\pi}{\sqrt{\omega_\beta^2 - \beta^2}} \approx 4$, and the factor of this excitation is

$$\alpha_e = 1 + \frac{\delta y - y_0}{\delta y} e^{-\pi/\sqrt{(\frac{\omega_\beta}{\beta})^2 - 1}}.$$

For $y_0 = 0$, $\alpha_e \approx 1.67$. It is easy to show that the factor of first excitation for mean divergence is exactly $\alpha_e = 1 + e^{-\pi/\sqrt{(\frac{\omega_\beta}{\beta})^2 - 1}} \approx 1.67$, a value independent of initial offset.

Similarly, we model the first order moments in single frequency–based periodic misalignment case by replacing the constant driving term with $\delta y \cos(\omega t)$ in Eq. (32). The complete solution of this periodically driven harmonic oscillator is given by

$$\bar{y}(t) = A(\omega_\beta, \omega, \beta) \times \left[\cos(\omega t + \vartheta) - \frac{\cos\vartheta e^{-\beta t}}{\cos\psi} \cos\left(t\sqrt{\omega_\beta^2 - \beta^2} + \psi\right)\right] + \frac{y_0}{\cos\psi} e^{-\beta t} \cos\left(t\sqrt{\omega_\beta^2 - \beta^2} + \psi\right), \tag{34}$$

where

$$A(\omega_\beta, \omega, \beta) = |\delta y| \frac{\mathrm{sign}\left(-\frac{\omega_\beta^2}{\beta\omega} \delta y \sin\vartheta\right)}{\sqrt{\left(\frac{\omega_\beta^2 - \omega^2}{\omega_\beta^2}\right)^2 + \left(\frac{2\beta\omega}{\omega_\beta^2}\right)^2}}, \tag{35a}$$

$$\tan\vartheta = \frac{2\beta\omega}{\omega^2 - \omega_\beta^2}, \tag{35b}$$

and

$$\tan\psi = \frac{A(\omega_\beta, \omega, \beta)[\beta\cos\vartheta - \omega\sin\vartheta] - y_0' - \beta y_0}{y_0 - A(\omega_\beta, \omega, \beta)\cos\vartheta}. \tag{35c}$$

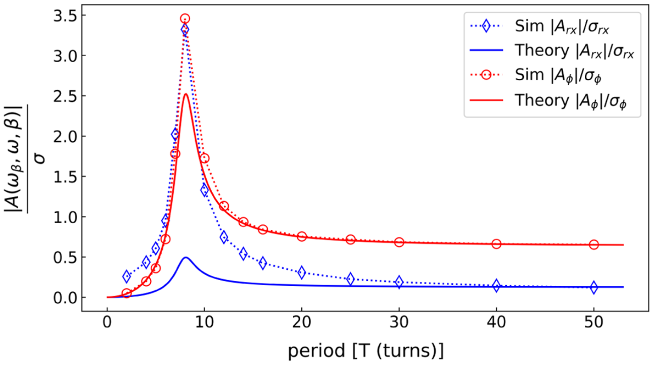

FIG. 10. Plots of normalized amplitude $|A(\omega_\beta, \omega, \beta)|$ with rms size versus misalignment periods in XFELO-A with $\beta = 0.1, \hat{q} = 4$, and crystal tilt amplitude of −45 nrad obtained from simulations (diamonds for position and circles for angle) and harmonic oscillator model (solid lines, blue for position, and red for angle) of Eq.(35).

Again, the value of phase ψ is determined from the initial conditions for $\bar{y}(0) = y_0$ and $\bar{y}'(0) = y_0'$. The first term is the steady-state solution, whereas the second and third terms are associated with the transient evolution of the first order moment that depends on the driving frequency and initial conditions, respectively. At steady state, the harmonic oscillator oscillates with the frequency of the driving source unlike the transient solutions. The appearance of frequency-dependent amplitude $A(\omega_\beta, \omega, \beta)$ represents the frequency response of the oscillator to the driving frequency and the excitation of the amplitude occurs close to the Betatron frequency. Moreover, the steady state itself represents oscillation about the driving amplitude (δy) in contrast to the static misalignment where a fixed orbit is achieved. As observed in the first two terms in Eq. (34), the transient excitation amplifies the driving amplitude, which may further enhance the frequency excitation leading to instabilities. Figure 10 depicts normalized frequency amplitudes of first order moments for various misalignment frequencies obtained from simulations (diamonds for position and circles for divergence) and harmonic oscillator model (sold lines) for XFELO-A with $\beta = 0.1, \hat{q} = 4$, and crystal tilt amplitude of −45 nrad after saturation. At steady state, the driving amplitude is manifested in the distorted orbit coordinates, $(-0.124\sigma_r, 0.634\sigma_\phi)$ for this case as found earlier in Sec. IV. The excitation of the amplitude near the Betatron period is clearly indicated by both simulations and the oscillator model of Eq. (35a). For the mean divergence, we find the harmonic oscillator model to reproduce the simulation results over the range of misalignment frequency/period. There is disagreement between the harmonic oscillator model and the simulations for the mean position when the misalignment frequency approaches Betatron frequency from either side. We note that the harmonic oscillator model is devoid of FEL dynamics and gain compensation. Moreover, the transient excitation of the misalignment amplitude may lead to slightly different driving amplitudes than predicted from the ray-transfer matrix analysis at these frequencies. In the next section, we will extend this frequency response analysis to estimate width of instabilities.

VII. INSTABILITIES

The intricacies involved in the modeling of XFELO make us rely on simulations to identify ranges of static or periodic misalignments that render XFELO performance unstable. Often, these studies would be on a case-by-case basis for individual XFELOs under consideration. These studies would not only be cumbersome, time consuming, and repetitive but also be rather limited in assessing overall performance and stability. In such studies, identifying patterns and limits often prove useful. For example, the upper threshold on misalignment frequency was easily determined using the sampling theorem (the Nyquist frequency limit), and two-fold frequency of power buildup was simply understood using the approximate gain model. Therefore, we apply the approximate Gaussian gain model, the lasing condition, and the harmonic analysis of the first order moments presented earlier to serve as the tools for exploring XFELO instability in the presence of static and single frequency driven periodic misalignments.

In the presence of time-dependent misalignments, the approximate Gaussian gain [Eq. (25)] takes the form

$$G(t) = G_0 e^{-[(\bar{r}(t)/a\Sigma_x)^2 + (\bar{\phi}(t)/b\Sigma_\phi)^2]/2}.$$

Since the FEL lasing is disturbed when $R(1 + G) \leq 1$, we substitute the gain from the above expression and $\hat{q} = \frac{R}{1-R}$ to obtain

$$\left(\frac{\bar{r}(t)}{a\Sigma_x}\right)^2 + \left(\frac{\bar{\phi}(t)}{b\Sigma_\phi}\right)^2 \geq 2\ln[G_0\hat{q}] \tag{36}$$

This is the required analytical expression that indicates when lasing becomes unachievable in the presence of misalignment. For static misalignment and when approaching steady state to the driving amplitude, this condition reduces to

$$|\delta r| \geq a\Sigma_x\sqrt{2\ln[G_0\hat{q}]}, \quad \text{for } \delta\phi = 0. \tag{37a}$$

$$|\delta\phi| \geq b\Sigma_\phi\sqrt{2\ln[G_0\hat{q}]}, \quad \text{for } \delta r = 0. \tag{37b}$$

For nonzero δr and $\delta\phi$, and $\frac{|\delta r|}{|\delta\phi|} = c$, we get

$$|\delta r| \geq \frac{abc\Sigma_x\Sigma_\phi}{\sqrt{(a\Sigma_x)^2 + (bc\Sigma_\phi)^2}}\sqrt{2\ln[G_0\hat{q}]}. \tag{38}$$

In other words, FEL lasing disturbance in the presence of the static misalignment is determined by the misalignment

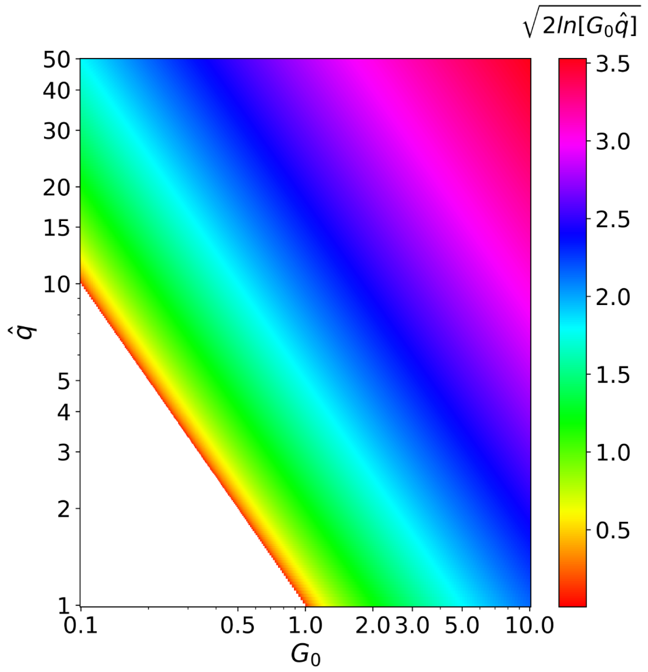

FIG. 11. Density plot of threshold value $\sqrt{2\ln[G_0\hat{q}]}$ for static misalignment for various $\hat{q}$ and G_0 values. Both x axis and y axis are on a $\log_{10}$ scale.

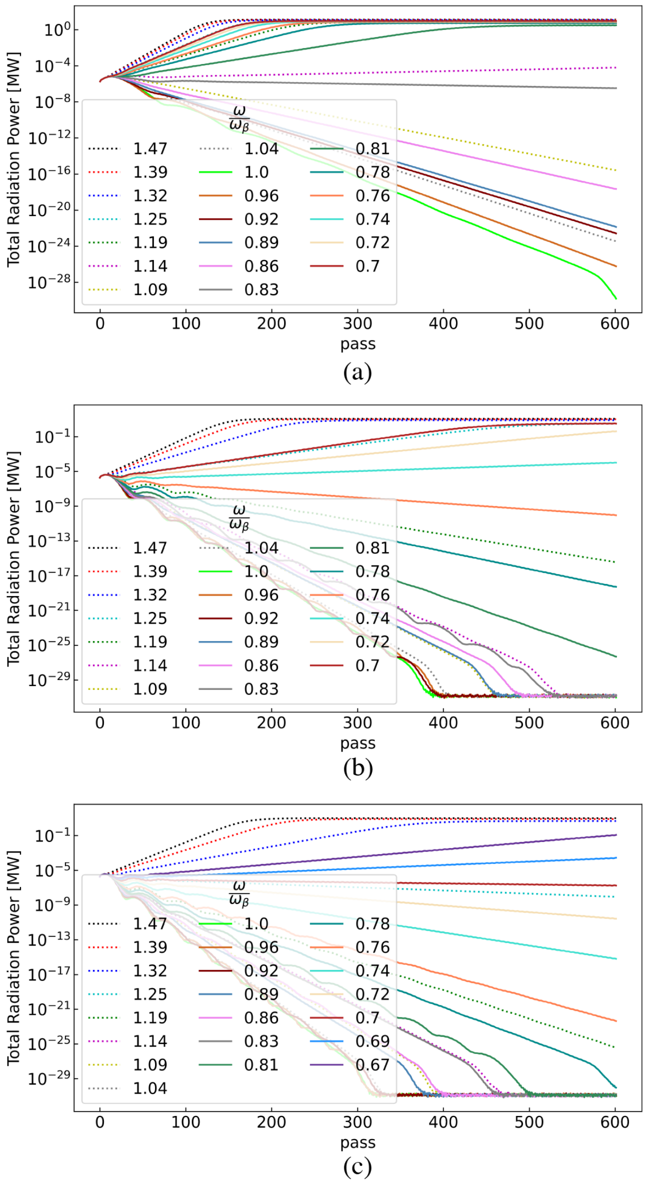

(a)

(b)

(c)

FIG. 12. Power evolution in XFELO-A with $R = 0.8$ $(\hat{q} = 4)$ subject to periodic misalignments with frequencies between 0.67 and 1.46 times the Betatron frequency with the crystal tilt amplitude of (a) 45 nrad, (b) 67.5 nrad, and (c) 78.75 nrad. The y-axis scale is $\log_{10}$.

amplitudes whose threshold depends on the convolved spatial and angular rms values as well as the ideal gain and cold cavity quality parameter (since $\hat{q} = \hat{Q}_c/\omega_\beta$). We note that the early excitation (as observed in Fig. 9) of the first order moments may exceed the threshold values for static misalignments right after the XFELO is turned on, which may render lasing difficult or even impossible. For XFELO-A, lasing is ensured for static misalignments if and only if the first order moments of the radiation beam do not approach and exceed half of the threshold values determined by conditions (37) and (38); Fig. 11 shows the density plot of the threshold values for a range of $\hat{q}$ and ideal gain values. High quality cavities (with higher $\hat{q}$ values > 10) are found to have higher threshold even for an ideal FEL system with $G_0 < 1$. Similarly, higher gain FEL permits adopting cavities with low $\hat{q}$ values for higher outcoupling.

In addition to depending on misalignment amplitudes and their excitations, instabilities under periodic misalignments also depend on the driving frequency as observed from the frequency excitations in Fig. 10. Figure 12(a) shows the power evolution in XFELO-A, with $R = 0.8(\hat{q} = 4)$, subject to periodic misalignments with frequencies between $0.7\omega_\beta$ and $1.47\omega_\beta$ for a crystal tilt amplitude of -45 nrad. We observe the instabilities to occur with a frequency width of $\delta\omega/\omega_\beta = 0.345 \pm 0.035$ between $0.81\omega_\beta$ and $1.19\omega_\beta$. This range is calculated by subtracting the upper and lower frequencies at which instability is observed (assuming power did not reach 0.1 MW by 600 turns). This difference is then centralized to account for the scan gaps with an adjusted error by half of the scan gaps. The resonance width increased to $\delta\omega/\omega_\beta \sim 0.49 \pm 0.04$ between $0.72\omega_\beta$ and $1.25\omega_\beta$ upon increasing the crystal tilt to -67.5 nrad as shown in Fig. 12(b). When the crystal was tilted by -78.75 nrad (1.75 amplification), the resonance width became $\delta\omega/\omega_\beta = 0.605 \pm 0.045$ between $0.67\omega_\beta$ and $1.32\omega_\beta$ [see Fig. 12(c)].

Similarly, we conducted single frequency scans for XFELO-A with different reflectivity (R) to observe the effect on resonance widths. Upon changing the reflectivity

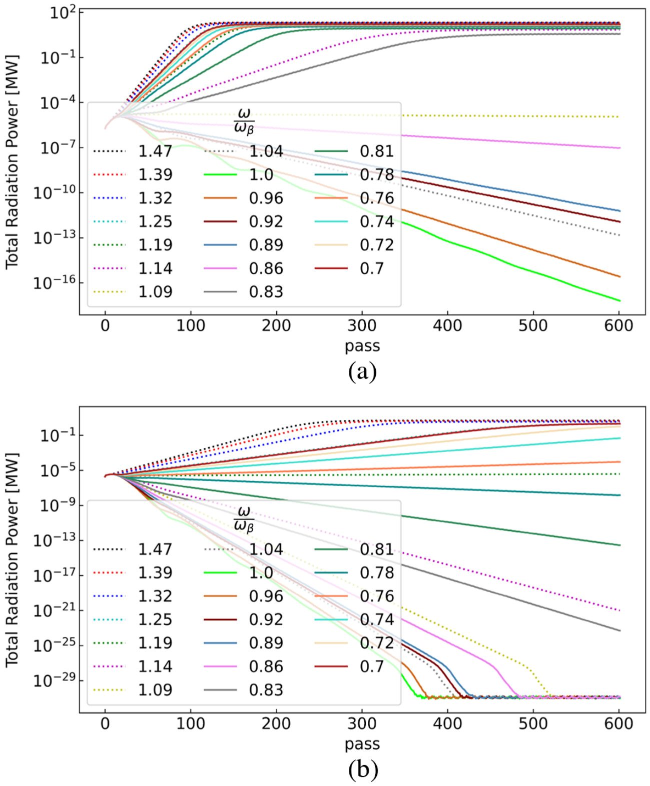

(a)

(b)

FIG. 13. Power evolution in XFELO-A with (a) $R = 0.8333$ ($\hat{q} = 5$), and (b) $R = 0.75$ ($\hat{q} = 3$) subject to periodic misalignments with single frequency between 0.77 and 1.46 times the Betatron frequency with an amplitude of crystal tilt of −45 nrad. The y axis is on a $\log_{10}$ scale.

of the XFELO cavity to $R = 0.8333$ so that $\hat{q} = 5$, we observed the instability width reduced to $\delta\omega/\omega_\beta = 0.27 \pm 0.04$ between $0.83\omega_\beta$ and $1.14\omega_\beta$ as shown in Fig. 13(a). Then, we lowered the cold cavity parameter to $\hat{q} = 3$ by setting $R = 0.75$. As shown in Fig. 13(b), the instability width widened to $\delta\omega/\omega_\beta = 0.47 \pm 0.04$ between $0.74\omega_\beta$ and $1.25\omega_\beta$

In the above case studies, a more accurate estimation of the frequency range for XFELO instability would require performing simulations of more frequency scans with smaller gaps. Alternatively, we can extend the expression of Eq. (36) to periodic misalignments to estimate the frequency range (resonance width) of instability. Using the amplitude part and ignoring the oscillating component from Eq. (34), we get

$$\left(\frac{A_r(\omega_\beta, \omega, \beta)}{a\Sigma_x}\right)^2 + \left(\frac{A_\phi(\omega_\beta, \omega, \beta)}{b\Sigma_\phi}\right)^2 \geq 2\ln[G_0\hat{q}]. \tag{39}$$

Substituting $|A_y(\omega_\beta,\omega,\beta)| = |\delta y|\omega_\beta^2[(\omega_\beta^2 - \omega^2)^2 + (2\beta\omega)^2]^{-1/2}$ into the above expression, we obtain the frequency range or width of the instability given by

$$\frac{\delta\omega}{\omega_\beta} = \sqrt{1 - \frac{2\beta^2}{\omega_\beta^2} + \frac{1}{2}F} - \sqrt{1 - \frac{2\beta^2}{\omega_\beta^2} - \frac{1}{2}F}, \tag{40a}$$

$$F = \sqrt{\left(\frac{2\beta}{\omega_\beta}\right)^4 - 4\left(\frac{2\beta}{\omega_\beta}\right)^2 + 2\frac{(\delta r/a\Sigma_x)^2 + (\delta\phi/b\Sigma_\phi)^2}{\ln[G_0\hat{q}]}} \tag{40b}$$

The textbook approach to approximate the resonance width relies on solving for full-width at half maximum (FWHM) of $|A_r(\omega_\beta, \omega, \beta)|^2$ and is equal to 2β to first order in β for optical cavities with $\beta \ll \omega_\beta$ [35]. We follow Jose and Saletan [35] to define a new parameter $\hat{Q}$, which represents the effective quality of XFELO cavities for these damped oscillations and the sharpness of the resonance peak, where $\hat{Q} = \frac{\omega_\beta}{2\beta} = \frac{\omega_\beta}{1-R}$ to first order in β. The equivalent cold cavity quality parameter in the absence of FEL gain would be $\hat{Q}_c = R\hat{Q} = \omega_\beta\hat{q}$. Then, we can effectively write the FWHM width of the resonance for a cold cavity by

$$\left(\frac{\delta\omega}{\omega_\beta}\right)_c = \frac{2\beta}{\omega_\beta} = \frac{1}{\hat{Q}_c} = \frac{1}{\omega_\beta\hat{q}}. \tag{41}$$

The FWHM formulas for resonance width are useful to identify the extent of unstable regions based only on the information of Betatron frequency and reflectivity or the cold cavity quality parameter of XFELOs under study. From Eq. (41), we find FWHM widths in XFELO-A to be $(\delta\omega/\omega_\beta)_c \approx 0.32$ for $\hat{q} = 4$, ≈0.25 for $\hat{q} = 5$, and ≈0.42 for $\hat{q} = 3$. While these estimates are not far from the resonance widths we obtained from simulations in Figs. 12 and 13 for the crystal tilt amplitude of 45 nrad, formulae (41) does not indicate any truncation or expansion of the resonance width when the misalignment amplitude is altered. This shortcoming is addressed by formulas (40), which includes the misalignment amplitudes in the expression for resonance width. Figure 14 shows the excitation curves obtained from this calculation for case studies of Figs. 12 and 13 with $\beta = (1 - R)/2$ from Eq. (40). The instability is set for normalized amplitude equal to 1 and resonance widths obtained from this calculation are slightly smaller than the values recovered from the simulation studies earlier for various $\hat{q}$ values and applied misalignment amplitudes. This discrepancy could be the result of observed differences in frequency response between simulations and the harmonic oscillator model we discussed earlier (see Fig. 10). Nevertheless, the trend of decreasing/increasing resonance widths with increasing $\hat{q}$/misalignment amplitudes is clearly observed.

Table II summarizes resonance widths obtained from simulations and theoretical approximations of Eqs. (40) and (41) for all XFELOs of Table I. The trend of decreasing and increasing resonance widths with a respective increase in $\hat{q}$

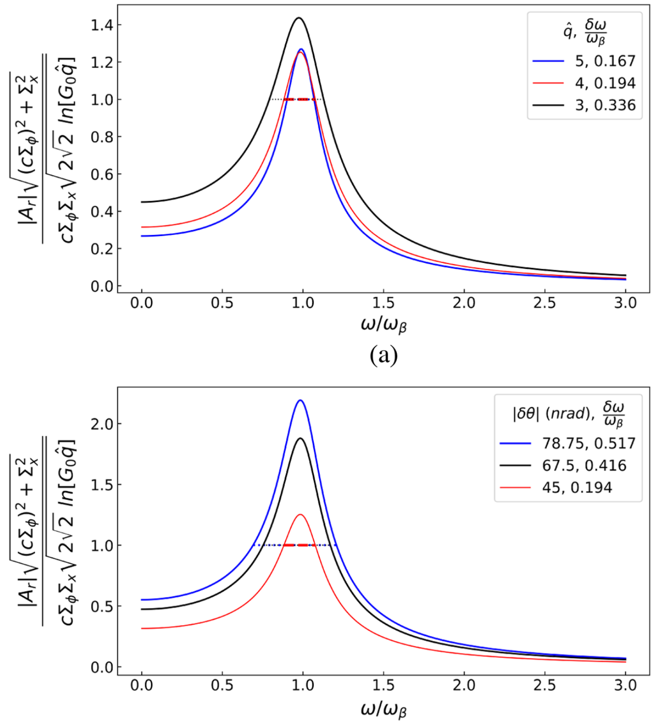

(a)

(b)

FIG. 14. Normalized excitation amplitude plotted against normalized frequency for the periodic misalignment of case studies of (a) Fig. 13 for cavities with $\hat{q}=3$, $\hat{q}=4$, and $\hat{q}=5$ and (b) Fig. 12 in which crystal tilt of amplitude 45 nrad is amplified by a factor of 1.5 and 1.75. The resonance frequency widths are obtained when normalized excitation equals 1 based on Eq. (40), beyond which instability kicks in.

TABLE II. Comparison of resonance widths obtained from simulations and analytical formula of Eqs. (40) and (41).

$\hat{q}=\frac{R}{1-R}$	Crystal Offset (δx μm, $\delta\theta$ μrad)	Simulations ($\delta\omega/\omega_\beta$)	Theory ($\delta\omega/\omega_\beta$)	FWHM $(\delta\omega/\omega_\beta)_c$
XFELO-A:	$\omega_\beta \approx 0.79$	$G_0 = 0.44$		
4	(0, −0.045)	0.345 ± 0.035	0.194	0.32
4	(0, −0.0675)	0.49 ± 0.04	0.416	⋯
4	(0, −0.07875)	0.605 ± 0.045	0.517	⋯
5	(0, −0.045)	0.27 ± 0.04	0.167	0.25
3	(0, −0.045)	0.47 ± 0.04	0.336	0.42
XFELO-C:	$\omega_\beta \approx 1.65$	$G_0 = 1.03$		
4	(−15, 0)	0.17 ± 0.04	0.152	0.15
4	(−22.5, 0)	0.36 ± 0.04	0.267	⋯
4	(−26.25, 0)	0.39 ± 0.04	0.32	⋯
5	(−15, 0)	0.085 ± 0.045	0.15	0.12
2.5	(−15, 0)	0.27 ± 0.04	0.164	0.24
XFELO-B:	$\omega_\beta \approx 1.65$	$G_0 = 1.48$		
4	(−20, 0.04)	0.17 ± 0.04	0.223	0.15
4	(−30, 0.06)	0.42 ± 0.04	0.374	⋯
4	(−35, −0.07)	0.495 ± 0.045	0.446	⋯
5	(−20, 0.04)	0.085 ± 0.045	0.222	0.12
2.5	(−20, 0.04)	0.3 ± 0.04	0.248	0.24

and misalignment amplitudes are effectively observed from both theory and simulations. In simulation studies of XFELO-A, the resonance widths estimated from theory are found to be slightly smaller than simulation values. For XFELO-C, the estimated resonance widths from the simulation are found to be slightly larger compared to the theoretically calculated values from Eq. (40). On the other hand, the FWHM width formulas predict similar widths obtained from simulations for various $\hat{q}$ with driving misalignment amplitude corresponding to displacement error of −15 μm of the first crystal. This crystal displacement results in the radiation beam offset at the waist by approximately $(0.76\sigma_r, 0.82\sigma_\phi)$ from the original optical axis with the driving amplitude of $(-0.00001\sigma_r, 0.758\sigma_\phi)$ at the steady state. Although XFELO-B has higher FEL gain than XFELO-C, the FWHM resonance widths from formulas (41) are the same for cavities with same $\hat{q}$ values because they have same Betatron frequency. The predicted FWHM widths are also found to be similar for XFELO-B when the first crystal is displaced by −20 μm and tilted by 40 nrad, resulting in the radiation beam offset of approximately $(1.16\sigma_r, 0.87\sigma_\phi)$ at the waist from the optical axis with the corresponding driving amplitude of $(0.178\sigma_r, 0.972\sigma_\phi)$. Again, we find the resonance widths estimated from Eq. (40) to be slightly different than that obtained from simulations for XFELO-B as well. We note that we used the same damping factor $\beta = \frac{1-R}{2}$ in all of these calculations of the theoretical estimates. Since XFELO-B and XFELO-C have the same Betatron frequency but different ideal FEL gains, it is feasible that higher FEL gain resulted in a lower damping factor. The accurate quantitative prediction of such a shift would require a large parameter scan studies and is beyond the scope of this article. Nevertheless, it is understood that the excitation of the misalignment amplitude and resonance width of instability can be reduced to a certain extent by choosing a cavity with a larger Betatron frequency and switching to a slightly higher FEL gain.

VIII. CONCLUSION

To sum up, we have presented a complete model for XFELO modeling within the paradigm of paraxial approximation for optical cavities with broadband optical elements, whose angular acceptance ≫μrad. We have incorporated methods and tools that allow us to simulate transverse misalignments and their effects in XFELOs with sufficient accuracy. We have studied the effects of transverse misalignment in XFELOs and the emergence of various phenomena due to the XFELO response. Static misalignment results in the reduction of single pass FEL gain and may result in nonlasing through early excitations. XFELOs can be made resilient to static misalignment and their excitations by either reducing outcoupling and loss in the cavity or switching to higher FEL gain without affecting outcoupling. The highest frequency of the oscillatory misalignment is limited by the Betatron frequency of the XFELO cavity due to folding. Power fluctuations due to higher frequencies are effectively damped, albeit resulting in a reduced overall power output. Large frequencies, greater than twice the Betatron frequencies, and their excitations are not worrisome. Although smaller frequencies do not lead to instabilities, the power output fluctuations are imprinted from the misalignment effects. In other words, larger misalignment amplitudes at lower frequencies will affect XFELO output badly. Such effects should be mitigated through precise alignment and active feedback control. Finally, the regions of instability for static and single frequency oscillatory misalignment can be predicted by exploiting Gaussian gain model and driven harmonic oscillator models. The resonance widths can be adjusted by tuning Betatron frequency, cold cavity parameter $\hat{Q}_c$, and ideal FEL gain in the XFELO.

ACKNOWLEDGMENTS

This work is based on research supported by U.S. Department of Energy Office of Science-Basic Energy Sciences under Contract No. DE-AC02-06CH11357. The authors appreciate encouraging and consistent feedback from Kwang-Je Kim (University of Chicago/Argonne Laboratory) in several aspects of this project. We also thank Steven Kearny at Argonne Laboratory for discussions on high frequency noise sources.

APPENDIX A: FREE-SPACE PROPAGATION

Free-space propagation of the Gauss-Hermite mode coefficients comes into play when we implement misalignment projection, time dependency, or slippage in FEL simulations. For single frequency component in one dimension, we can solve for the free-space propagation in angular space by

$$\tilde{E}(\phi; z) = e^{-ik\frac{\phi^2}{2}(z-z_0)}\tilde{E}(\phi; z_0), \tag{A1}$$

where z_0 is the starting position and z is the position of interest at which we want to compute the field. We have dropped the constant phase $k(z - z_0)$ for convenience. The tilde denotes the field expansion in angular space, defined by the Fourier transform of the field in the coordinate space, i.e.,

$$\begin{aligned}\tilde{E}(\phi; z) &= \frac{1}{\lambda}\int dr\, e^{-ik\phi r}E(r; z) \\ &= \int dr\, e^{-ik\phi r}\sum_l \mathcal{E}_l(z)\frac{\mathrm{Exp}\left[-\frac{r^2(1-iz/z_R)}{4\sigma_r^2(1+z^2/z_R^2)}\right]}{\sqrt{2^l l!\sigma_r(1+z^2/z_R^2)^{1/2}}}H_l\left[\frac{r/\sigma_r}{\sqrt{2(1+z^2/z_R^2)}}\right]e^{-i(l+1/2)\mathrm{atan}(z/z_R)},\end{aligned} \tag{A2}$$

where we substituted $E(x; z)$ from Eq. (1) and kept only the modes in one transverse direction. We can solve the above expression using integral properties of Hermite polynomial generating function to obtain the one-dimensional field in angular space

$$\tilde{E}(\phi; z) = \sum_l \mathcal{E}_l(z)\tilde{M}_l(\phi), = \sum_l \mathcal{E}_l(z)\frac{(-i)^l}{\sqrt{\lambda\sigma_\phi 2^l l!}}e^{-\frac{\phi^2}{4\sigma_\phi^2}(1+i\zeta)}H_l\left[\frac{\phi}{\sqrt{2}\sigma_\phi}\right], \tag{A3}$$

where $\sigma_{x'} = \sigma_\phi$ and $\zeta = z/z_R$. Now, we can apply field expression from Eq. (A3) in Eq. (A1) and use mode projection to obtain the expression for outgoing mode coefficients. Using projection, integration, $\varphi = \frac{\phi}{\sqrt{2}\sigma_\phi}$, and $z_R = \frac{1}{2k\sigma_\phi^2}$, we get

$$\begin{aligned}\mathcal{E}_n(z) &= \sum_l \mathcal{E}_l(z_0)\frac{i^{3l+n}}{\sqrt{\pi 2^{l+n} l!n!}}\int d\varphi e^{-ik\varphi^2\sigma_\phi^2(z-z_0)}e^{-\varphi^2[1+i(\zeta_0-\zeta)/2]}H_l(\varphi)H_n(\varphi) \\ &= \sum_l \mathcal{E}_l(z_0)\frac{i^{3l+n}}{\sqrt{\pi 2^{l+n} l!n!}}\int d\varphi e^{i\varphi^2(\zeta_0-\zeta)/2}e^{-\varphi^2[1+i(\zeta_0-\zeta)/2]}H_l(\varphi)H_n(\varphi) \\ &= \sum_l \mathcal{E}_l(z_0)\frac{i^{3l+n}}{\sqrt{\pi 2^{l+n} l!n!}}\int d\varphi e^{-\varphi^2}H_l(\varphi)H_n(\varphi) \\ &= \sum_l \mathcal{E}_l(z_0)\frac{i^{3l+n}}{\sqrt{\pi 2^{l+n} l!n!}}2^n n!\sqrt{\pi}\delta_{n,l} = \mathcal{E}_n(z_0).\end{aligned} \tag{A4}$$

This shows that the Gauss-Hermite field mode coefficients remain constant under free-space propagation besides accumulating the constant phase.

APPENDIX B: ABCD PROPAGATION

We follow Siegman [20] to derive the effect of ABCD matrix on the propagation of Gauss-Hermite modes of Eq. (1b). Let us define the complex beam parameter q as

$$\frac{1}{q(z)} = \frac{1}{R(z)} + \frac{2i}{kw^2(z)},$$

where $R(z) = z[1 + (z_R/z)^2]$ is the radius of curvature, and $w(z) = 2\sigma_r\sqrt{1 + (z/z_R)^2}$ is the waist size at any position z. Then, the field amplitude of the unnormalized nth transverse mode reduces to

$$u_n(r; z) = \alpha_n w^n(z) \mathrm{Exp}\left[\frac{ikr^2}{2q(z)}\right] H_n\left(\frac{r\sqrt{2}}{w(z)}\right). \tag{B1}$$

The output of this Gauss-Hermite mode after passing through an ABCD system is solved using Huygen's integral for wave propagation and is given by

$$u_n(r_2) = e^{ikL} \int dr_1 K(r_2, r_1) u_n(r_1), \tag{B2}$$

where the ABCD kernel of propagation is

$$K(r_2, r_1) = \frac{1}{\sqrt{iB\lambda}} \mathrm{Exp}\left[\frac{ik}{2B}(Ar_1^2 - 2r_2r_1 + Dr_2^2)\right],$$

and L is the length of the ABCD system [20]. Since kL is fixed in the context of this report and presented analysis, we ignore the phase prefactor of L and solve Eq. (B2) to get

$$u_n(r_2; z) = \alpha_{n,2} w_2^n(z) \mathrm{Exp}\left[\frac{ikr_2^2}{2q_2(z)}\right] H_n\left(\frac{r_2\sqrt{2}}{w_2(z)}\right),$$

where the new mode coefficient, new waist size, and the new complex beam parameter take the following form:

$$\alpha_{n,2}(z) = \alpha_n(z)\left(A + \frac{B}{q(z)}\right)^{-(n+\frac{1}{2})}, \tag{B3a}$$

$$w_2^2(z) = \left[w^2(z)\left(A + \frac{B}{q(z)}\right) - \frac{4iB}{k}\right]\left(A + \frac{B}{q(z)}\right), \tag{B3b}$$

and

$$\frac{1}{q_2(z)} = \frac{1}{B}\left(D - \frac{q(z)}{Aq(z) + B}\right). \tag{B3c}$$

Since $AD - BC = 1$, in general, the expression for the outgoing complex beam factor q_2 reduces to the well-known expression

$$q_2(z) = \frac{Aq(z) + B}{Cq(z) + D}. \tag{B4}$$

In the fourth paragraph of Sec. II B, we mentioned that for periodic cavities, the required criterion for stability of periodic cavities is $|\frac{A+D}{2}| < 1$, the result which one could easily arrive at by solving for eigenvalues in periodic resonators. There was no indication of additional constraints or requirements. For a Gaussian mode beam to propagate in such a stable periodic cavity, Eq. (B4) indicates that the complex beam parameter q be self-consistent from one turn to the next (i.e., $q_2 = q_1$). Once we solve for the self-consistent complex beam parameter from Eq. (B4), which gives

$$\frac{1}{q_{+/-}} = \frac{D - A}{2B} \pm \frac{i}{B}\sqrt{1 - \left(\frac{A + D}{2}\right)^2}, \tag{B5}$$

we perturb the incoming beam parameter by a tiny quantity δq to observe its effects on the outgoing parameter. Keeping the terms upto first order in δq after expansions, the outgoing parameter becomes

$$q_2 = \frac{Aq_1 + B}{Cq_1 + D} + \frac{\delta q}{(Cq_1 + D)^2}.$$

When we substitute the self-consistent property (i.e., $q_2 = q_1$) in the perturbation term, we obtain

$$q_2 = q_2 + \delta q_2 = q_2 + \frac{\delta q}{(A + B/q_1)^2}. \tag{B6}$$

Based on the above expression, the stability of the beam parameter depends on the growth rate of second term, $(A + B/q)$ in particular. For the self-consistent parameter of Eq. (B5), this expression takes the form

$$A + \frac{B}{q_{+/-}} = e^{i\,\mathrm{sign[B]}\varphi}, \tag{B7}$$

where $\varphi = \mathrm{acos}[\frac{A+D}{2}]$. We replaced the signs of stable eigenvalue by the sign of B component because a real spot size (and therefore the stable eigenvalue) in Eq. (B5) is decided by the sign of B. The definition of the beam parameter suggests that for $|(\frac{A+D}{2})| < 1$, the optical cavity will have a confined and stable mode with a real waist size; in such cavity systems, the perturbations oscillate about a fixed orbit and hence, are perturbations stable as well as geometrically stable [as discussed in geometric optics of Sec. II B]. Such systems define a radius of curvature given by $R = \frac{2B}{D-A}$ and Rayleigh range $z_R = |B|/\sqrt{1 - (A + D)^2/4}$ for a self-consistent Gauss-Hermite mode. If $|(\frac{A+D}{2})| \geq 1$, the system is rendered unstable as

$A+\frac{B}{q_{+/-}}=e^{\pm\bar{\varphi}}$ grows/decays exponentially for unstable eigenvalues with $\bar{\varphi}=\mathrm{acosh}[\frac{A+D}{2}]$.

For stable and periodic ABCD transport system with the self-consistent beam parameter defined for Gauss-Hermite modes, each field mode accumulates modal phase upon passing through it. The phase accumulated by a one-dimensional field with mode number n per turn is given by

$$\frac{\alpha_{n,2}}{\alpha_n}=\left(A+\frac{B}{q_{+/-}}\right)^{-(n+\frac{1}{2})} \\ =e^{-i(n+1/2)\mathrm{sign}[\mathrm{B}]\mathrm{acos}[\frac{A+D}{2}]}. \tag{B8}$$

An alternate derivation of the accumulated phase shift for Gaussian beams has been derived in Ref. [36] and discussed thoroughly by Arai [37].

APPENDIX C: MISALIGNMENT PROJECTION

From Eq. (16), we have

$$\mathcal{P}_{n,l}(r_r,\phi_r) \\ =\frac{1}{\sqrt{2\pi}}\int dre^{ik(r-r_r)\phi_r}M_l(r-r_r;L_u/2)M_n^*(r;L_u/2) \\ =\frac{e^{-ikr_r\phi_r}}{\sqrt{\pi 2^{n+l}n!l!}}\int dye^{i\kappa y}e^{-[y^2+(y-Y_r)^2]/2}H_l(y-Y_r)H_n(y) \\ =\frac{e^{-(i\kappa Y_r+Y_r^2/2)}e^{(i\kappa+Y_r)^2/4}}{\sqrt{\pi 2^{n+l}n!l!}}\int dye^{-[y^2-(i\kappa+Y_r)/2]^2} \\ \times H_l(y-Y_r)H_n(y), \tag{C1}$$

where we have substituted

$$\kappa=\sqrt{2}k\sigma_r\phi_r,\qquad y=\frac{r}{\sigma_r\sqrt{2}},\quad \text{and}\quad Y_r=\frac{yr_r}{r}.$$

Let $p=y-(i\kappa+Y_r)/2$, then $dp=dy$. Similarly, for $\alpha=(Y_r+i\kappa)/2$ and $\beta=(i\kappa-Y_r)/2$, we get $y=p+\alpha$ and $y-Y_r=p+\beta$. Substituting these values in (C1), the integral takes the well-known form for Hermite polynomials (tabulated in Ref. [38])

$$\int dye^{-[y-(i\kappa+Y_r)/2]^2}H_l(y-Y_r)H_n(y) \\ =\int dpe^{-p^2}H_l(p+\beta)H_n(p+\alpha) \\ =\begin{cases} 2^n\sqrt{\pi}l!(\alpha)^{n-l}L_l^{n-l}(-2\alpha\beta), & [l\le n] \\ 2^l\sqrt{\pi}n!(\beta)^{l-n}L_n^{l-n}(-2\alpha\beta), & [n\le l]. \end{cases} \tag{C2}$$

Since $-2\alpha\beta=(\kappa^2+Y_r^2)/2$ and $e^{-(i\kappa Y_r+Y_r^2/2)}e^{(\frac{i\kappa+Y_r}{2})^2}=e^{-i\kappa Y_r/2}e^{-(\kappa^2+Y_r^2)/4}$, the misalignment projection matrix becomes

$$\mathcal{P}_{n,l}(r_r,\phi_r) \\ =e^{-i\kappa Y_r/2}e^{-(\kappa^2+Y_r^2)/4} \\ \times\begin{cases} \sqrt{\frac{l!}{n!}}\left(\frac{i\kappa+Y_r}{\sqrt{2}}\right)^{n-l}L_l^{n-l}\left(\frac{\kappa^2+Y_r^2}{2}\right), & [l\le n] \\ \sqrt{\frac{n!}{l!}}\left(\frac{i\kappa-Y_r}{\sqrt{2}}\right)^{l-n}L_n^{l-n}\left(\frac{\kappa^2+Y_r^2}{2}\right), & [n\le l]. \end{cases} \tag{C3}$$

When we rewrite the above expression in terms of r_r and ϕ_r by substituting $Y_r=r_r/(\sigma_r\sqrt{2})$, $\kappa=k\sigma_r\phi_r\sqrt{2}=z_R\phi_r/(\sigma_r\sqrt{2})$, and $z_R=\sigma_r/\sigma_{r'}=2k\sigma_r^2$, we arrive at Eq. (17).

[1] T. Kolodziej, Y. Shvyd'ko, D. Shu, S. Kearney, S. Stoupin, W. Liu, T. Gog, D. A. Walko, J. Wang, A. Said, T. Roberts, K. Goetze, M. Baldini, W. Yang, T. Fister, V. Blank, S. Terentyev, and K.-J. Kim, J. Synchrotron Radiat. **25**, 1022 (2018).

[2] T. Kolodziej, S. Stoupin, W. Grizolli, J. Krzywinski, X. Shi, K.-J. Kim, J. Qian, L. Assoufid, and Y. Shvyd'ko, J. Synchrotron Radiat. **25**, 354 (2018).

[3] G. Marcus *et al.*, in *Proceedings of the 39th International Free-Electron Laser Conference, FEL 2019, Hamburg, Germany* (JACoW, Geneva, Switzerland, 2019), p. 282.

[4] P. Rauer, I. Bahns, W. Hillert, J. Rossbach, W. Decking, and H. Sinn, in *Proceedings of the 39th International Free-Electron Laser Conference, FEL 2019, Hamburg, Germany* (JACoW, Geneva, Switzerland, 2019), p. 62.

[5] I. Agapov, Y. Chae, and W. Hillert, in *Proceedings of the 9th International Particle Accelerator Conference, IPAC-2018, Vancouver, BC, Canada* (JACoW, Geneva, Switzerland, 2018), Vol. 1420.

[6] K.-J. Kim, Y. Shvyd'ko, and S. Reiche, Phys. Rev. Lett. **100**, 244802 (2008).

[7] R. Colella and A. Luccio, Opt. Commun. **50**, 41 (1984).

[8] D. A. G. Deacon, L. R. Elias, J. M. J. Madey, G. J. Ramian, H. A. Schwettman, and T. I. Smith, Phys. Rev. Lett. **38**, 892 (1977).

[9] C. A. Brau, *Free Electron Lasers* (Academic Press, New York, 1990).

[10] T. Kolodziej and T. Maxwell, Synchrotron Radiat. News **29**, 31 (2016).

[11] B. Adams *et al.*, Scientific opportunities with an X-ray Free-Electron Laser Oscillator, arXiv:1903.09317.

[12] Z. Huang and R. D. Ruth, Phys. Rev. Lett. **96**, 144801 (2006).

[13] S. Reiche, Nucl. Instrum. Methods Phys. Res., Sect. A **429**, 243 (1999).

[14] W. M. Fawley, A user manual for GINGER and its post-processor XPLOTGIN, Lawrence Berkeley National Laboratory, Technical Report No. LBNL-49625-Rev.1, 2004.

[15] R. R. Lindberg, in *Proceedings of the 39th International Free-Electron Laser Conference, FEL 2019, Hamburg, Germany* (JACoW, Geneva, Switzerland, 2019), p. 110.

[16] W. B. Colson and P. Elleaume, Appl. Phys. B **29**, 101 (1982).

[17] H. Freund, S. Biedron, and S. Milton, IEEE J. Quantum Electron. **36**, 275 (2000).

[18] E. Hemsing, A. Gover, and J. Rosenzweig, Phys. Rev. A **77**, 063831 (2008).

[19] G. T. Park, Performance-limiting factors for x-ray free electron laser oscillator as a highly coherent, high spectral purity x-ray source, Ph.D. Dissertation, University of Chicago, 2012.

[20] A. E. Siegman, *Lasers* (University Science Books, California, 1986).

[21] H. Kogelnik and T. Li, Appl. Opt. **5**, 1550 (1966).

[22] K.-J. Kim, Z. Huang, and R. Lindberg, *Synchrotron Radiation and Free-Electron Lasers: Principles of Coherent X-Ray Generation* (Cambridge University Press, Cambridge, England, 2017).

[23] Z. Huang and K.-J. Kim, Phys. Rev. ST Accel. Beams **10**, 034801 (2007).

[24] R. M. J. Cotterill, Appl. Phys. Lett. **12**, 403 (1968).

[25] K.-J. Kim and Y. V. Shvyd'ko, Phys. Rev. ST Accel. Beams **12**, 030703 (2009).

[26] Y. Shvyd'ko, Feasibility of x-ray cavities for free electron laser oscillators, International Committee for Future Accelerators, Technical Report No. 60, 2013.

[27] K.-J. Kim, Distorted optical axis in closed cavity, Advanced Photon Source, Argonne National Laboratory, Technical Report No. ANL/APS/LS-364, 2020 (originally released as AOP-TN-2020-106).

[28] J. L. Turner, C. Adolphsen, G. B. Bowden, F. J. Decker, S. C. Hartman, S. Matsumoto, G. Mazaheri, D. McCormick, M. Ross, R. Stege, S. Virostek, and M. Woodley, in *Proceedings of the Particle Accelerator Conference, Dallas, TX, 1995* (IEEE, New York, 1995), Vol. 1, p. 665.

[29] L. Zhang, Conf. Proc. C **960610**, 1359 (1996).

[30] A. Seryi, in *Proceedings of the Particle Accelerator Conference, Chicago, IL, 2001* (IEEE, New York, 2001) Vol. 1, p. 364.

[31] V. Vadim Sajaev, Z. Liu, J. Nudell, and C. Preissner, Calculation of orbit motion due to girder resonant vibration, Advanced Photon Source, Argonne National Laboratory, Technical Report No. AOP-TN-2017-065, 2017.

[32] R. R. Lindberg, K. J. Kim, Yu. Shvyd'Ko, and W. M. Fawley, Phys. Rev. ST Accel. Beams **14**, 010701 (2011).

[33] W. Qin, S. Huang, K. X. Liu, K. J. Kim, R. R. Lindberg, Y. Ding, Z. Huang, T. Maxwell, K. Bane, and G. Marcus, in *Proceedings of the 38th International Free-Electron Laser Conference, FEL 2019, Hamburg, Germany* (JACoW, Geneva, Switzerland, 2017), p. 247.

[34] S. Stoupin, F. Lenkszus, R. Laird, K. Goetze, K.-J. Kim, and Y. Shvyd'ko, Adaptive x-ray optics, in *Proceedings of SPIE, San Diego, CA, 2010*, edited by A. M. Khounsary, S. L. O'Dell, and S. R. Restaino (SPIE, Bellingham, WA, 2010), Vol. 7803.

[35] J. V. José and E. J. Saletan, Scattering and linear oscillations, in *Classical Dynamics: A Contemporary Approach* (Cambridge University Press, Cambridge, England, 1998), pp. 147–200.

[36] M. F. Erden and H. M. Ozaktas, J. Opt. Soc. Am. A **14**, 2190 (1997).

[37] K. Arai, On the accumulated round-trip Gouy phase shift for a general optical cavity, Laser Interferometer Gravitational Wave Observatory, Technical Report No. LIGO-T1300189-v1, 2013.

[38] I. Gradshteyn and I. Ryzhik, in *Table of Integrals, Series, and Products*, 7th ed., edited by A. Jeffrey and D. Zwillinger (Academic Press, Boston, MA, 2007), pp. 631–857.